Article

Design, Multi-Perspective Computational Investigations, and Experimental Correlational Studies on Conventional and Advanced Design Profile Modified Hybrid Wells Turbines Patched with Piezoelectric Vibrational Energy Harvester Devices for Coastal Regions

Janani Thangaraj [1], Senthil Kumar Madasamy [1], Parvathy Rajendran [2,*], Safiah Zulkifli [2,*], Rajkumar Rajapandi [3], Hussein A. Z. AL-bonsrulah [4,5], Beena Stanislaus Arputharaj [6], Hari Prasath Jeyaraj [1] and Vijayanandh Raja [1]

1   Department of Aeronautical Engineering, Kumaraguru College of Technology, Coimbatore 641049, Tamil Nadu, India; vijayanandh.raja@gmail.com (V.R.)
2   School of Aerospace Engineering, Universiti Sains Malaysia, Engineering Campus, Nibong Tebal 14300, Pulau Pinang, Malaysia
3   Department of Mathematics, Kumaraguru College of Technology, Coimbatore 641049, Tamil Nadu, India
4   Mechanical Power Technical Engineering Department, Al-Amarah University College, Amarah 62001, Iraq
5   Department of Computer Techniques Engineering, Al Safwa University College, Karbala 56001, Iraq
6   Department of Research and Innovation, Saveetha School of Engineering, SIMATS, Chennai 602105, Tamil Nadu, India
*   Correspondence: aeparvathy@usm.my (P.R.); safiahzul@usm.my (S.Z.)

Abstract: This work primarily investigates the performance and structural integrity of the Wells turbines for power production in coastal locations and their associated unmanned vehicles. An innovative design procedure is imposed on the design stage of the Wells turbine and thus so seven different models are generated. In the first comprehensive investigation, these seven models underwent computational hydrodynamic analysis using ANSYS Fluent 17.2 for various coastal working environments such as hydro-fluid speeds of 0.34 m/s, 1.54 m/s, 12 m/s, and 23 m/s. After this primary investigation, the best-performing Wells turbine model has been imposed as the second comprehensive computational investigation for three unique design profiles. The imposed unique design profile is capable of enhancing the hydro-power by 15.19%. Two detailed, comprehensive investigations suggest the best Wells turbine for coastal location-based applications. Since the working environments are complicated, additional advanced computational investigations are also implemented on the best Wells turbine. The structural withstanding capability of this best Wells turbine model has been tested through coupled computational hydro-structural analysis for various lightweight materials. This best Wells turbine also enforces the vibrational failure factors such as modal and harmonic vibrational analyses. Finally, advanced and validated coupled engineering approaches are proposed as good methodology for coastal location-based hydropower applications.

Keywords: CFD; FEA; FSI; composite materials; hydro-energy; hybrid energy; forced and free vibrations

1. Introduction

The Wells turbine is a type of turbine that was built specifically for the purpose of harvesting energy from waves. The oscillating water column is the most common application for this material. The Wells turbine, which was designed by Prof. Alan Arthur Wells in Belfast and uses symmetrical blades, can convert the flow of air coming from either direction into the same direction as the turbine's spin. The angle of attack (α) is quite high, despite the fact that its efficiency is somewhat poor. The symmetrical airfoils that

are utilized in the construction of the Wells turbine blades are the root cause of the poorer efficiency as well as the high angle of attack. The capability of the Wells turbine to self-rectify the flow of incoming waves is one of the fundamental properties that distinguish it from other types of turbines. Additionally, the Wells turbine is a type of turbine design that has been developed expressly for use in wave energy converters. This design is both highly effective and adaptable, making it an excellent choice for this type of application. Because of its potential to work effectively in bidirectional flow and its ability to self-rectify under a diverse set of wave conditions, it is an excellent option for the generation of electrical power from ocean waves.

The turbine is able to function well despite shifts in either the direction or the magnitude of the waves. This is accomplished by the turbine by angling a set of curved blades in such a way that a pressure difference is created between the top and bottom surfaces of the blade as the wave travels over it. This pressure differential is what causes the blade to rotate, and the rotation is what drives the generator that converts the rotation into usable electrical power. High rotating speed and the ability to be directly connected with electrical generators are the two aspects of the Wells turbine that are considered to be its most important characteristics. It is expected that the Wells turbine will play an increasingly vital role in the development of wave energy technology as the world continues its search for new renewable energy sources.

Relevant Works

Wells turbines with automated multi-objective optimization have been designed. Torque and pressure loss were improved with OPAL++. The highest torque (G1) and the lowest stress drop coefficient (G2) played major roles in the achievement of the highest performance. Compared to its predecessor, the new turbine has a stall point of 0.3. Both the G1 and G2 turbines have better efficiency than the reference turbine [1]. For sub-oscillating flight, Wells turbines employed second-regulation and entropy technology in the form of blades. Computational fluid dynamics (CFD) analyses of NACA airfoils with a sinusoidal waft boundary have been performed. The efficiency of the second law was drastically impacted by the angle of attack. This effect was quantified by the NACA 0015 between 15 and 25 degrees of attack. Airfoil section local entropy viscosity can be predicted via numerical simulations. When considering entropy generation, the Reynolds number is crucial, and NACA0015 is more cost effective and uses less expensive alternative airfoils [2]. The authors' analyzed the coupled dynamics that included the aero-elastic and volatile feedback of the movable blades. The most promising configuration was selected based on the CFD results for reducing strain overall. The major outcome was that the total pressure drop is three times that of a hard, rapid, straight blade [3]. To better depict drift unsteadiness, a simpler, two-equation turbulence version was modified. Using the SST (shear stress transport) transient fluid solver and a two-equation turbulence model, Open FOAM evaluated the efficiency of a Wells turbine [4]. The Wells turbine's suction-slotted blades performed admirably. Four different suction slots were investigated. The pressure decrease caused by the turbine drift coefficient was greatest in slots 4 and 7. Three-slot turbines were efficient. A test was carried out on NACA 0015, and slots in the NACA 0015 airfoil model were also used [5]. Disc actuator blades investigated the evolution of the motor. The "interference factors" between a turbine rotor's series of blades and a single airfoil determined the rotor's carry behaviors also drag. There were greater air velocities inside the blade passages in the CFD studies with the thicker rotors [6]. Wells turbine performance modeling and layout optimization using computational fluid dynamics were performed. Wells turbine performance can be predicted with either an experimental, analytic, or CFD-based model. Converting power from W to T waves is simple and inexpensive. A Wells turbine is inferior to an impulse turbine. When compared to other airfoils, NACA0015 is more efficient and produced less global entropy. The proposed work was produced the more using manual vanes and W-Ts with several stages. The cost of improved W-T performance increases [7].

Slots on both sides of an airfoil and glued guiding vanes were used in Wells turbines to increase efficiency and torque. Torque was increased by the imposed turbine slots. The Wells turbine's manual vanes were optimized for speed, rotational autonomy, and resistance to stalling. This action demonstrated that manual vanes function more effectively upstream than downstream. Based on the calculations, the slotted turbine turned over more quickly. Productivity, usability, and initialization are all enhanced with slotted blades and manual vanes [8]. The authors' proposed turbine must operate between 0 and 90 degrees to accommodate the varying airflow needed to harness wave energy. The blades in a Wells turbine's cascade are perpendicular to the axis of rotation, are offset by 90 degrees, and make it difficult to float. Complex stalls with a wide field of view can be simulated [9]. Different blade profiles, including NACA0020, NACA0015, CA9, and HSIM 15-262123-1576, were studied. Circular motion of the Wind CA9 blade profiles with a rotor solidity of 0.64 were used in Wells turbines. Turbogenerators that rotate in a circle exhibited rapid flotation tendencies. The performance curve of constant drift was slowed down by low flow coefficients [10]. The performance of a lightweight Wells turbine in a cutting-edge sea wave energy system was evaluated. Analysis was possible when the three-dimensional Navier–Stokes equations were stabilized. Going with the flow is an incompressible mechanism in SST k-turbulence. The efficiency of a turbine can be predicted by simulating the end clearance [11]. Numerical and practical tests were conducted on a small, single-wing Wells turbine with high solidity and no guide vanes. NACA0015 blades with a constant chord were used in the prototype. After running normal incompressible Reynolds-averaged Navier–Stokes (RANS) equations via finite-element simulations in three dimensions, the numerical evaluation were completed. A relaxed decrease in torque and pressure was identified [12]. In that study, regenerative ventilation was being evaluated for the possible arrangement of a new experimental record by mounting a turbine atop an oscillating water column. The DC systems were powered by the turbine, in which a NACA0015-based design profile was imposed on blades. The waft coefficient should be less than 0.1, and the turbine's Reynolds number should be high [13]. Wells turbines make a lot of noise and failed to work very well at high waft coefficients. These issues are resolved by skewing and reshaping the blades of the booster turbine and the rotor. The turbine was distorted by the Gurney flaps. The efficiency of blade profiles was enhanced [14].

The performance of Wells turbines with and without many planes was evaluated. Biplanes used contra-rotating rotors, while monoplanes relied on manually operated vanes. There were trials of a biplane turbine with two shafts. When compared to a monoplane turbine with guiding vanes, the contra-rotating turbine had a similar operational range, but it performed better post-stall and could withstand a pressure-drift ratio that was one mile higher. High viscous losses in the turbine rotor are optimal for recovery [15]. Turbine blades were imposed with symmetrical airfoils that revolve around a central hub. Energy generation can be maximized by using the rotational speed control loop. The turbine only spins in one direction, although the fluid can go in either direction. The goal of installing the stress sensors has been achieved. The first sensor tracked strain, while the second tracked pressure decrease from the faster generator [16]. Energy production is restricted by factors such as the predictability of waves, the efficiency of devices, etc. By optimizing the sweep angles of the blades, the performance and efficiency of the Wells turbine could be increased via numerical optimization. This investigation was finished using the RANS equations and determined the effectiveness in terms of strain, torque, and also waft. The authors' maximized the torque factor, and cross-validation errors were reduced with the use of Kriging. Increases in both turbine height and torque resulted from redesigned blade waft coefficients [17]. The notable observations are as follows: blades on monoplane turbines typically have a 90-degree angle, a Reynolds number of 8×10^5, a Mach number of 0.4 at the tip, and a hub-to-tip ratio of 0.6. Blades, tip clearance, and gliding efficiency are all distinct. Drift can be anticipated with the help of torque. Convergence of solutions was hampered by the discrepancy between axial velocity and tangential tip [18]. In this study, the authors compared static stall to dynamic stall and operational design settings. Next, they took

take a theoretical and practical look at two different ratios of tip clearance to chord length, 0.0056 and 0.0111. Three-dimensional measurements of steady-state and pulsed flow were taken on Wells turbine prototypes. The rate at which a drift was occurring can modify the flow. Offshore utility REWEC3 seawalls were depicted as Wells turbines at a 1:10 scale. Gliding coefficients, torque, and strain drop were used to rate Wells turbines. Gliding became unsteady in the sinusoidal current. Performance of turbines was influenced by tip clearance [19]. Turbine performance was impacted by tip leaking glide. The investigation of the drift of turbine blades was executed. An NACA 0020 bladed Wells turbine was analyzed using CFD solver called FLUENT. The ratio of tip clearance to chord length grew, which negatively affected turbine performance and positively impacted glide coefficient. Turbine stall was brought on by boundary layer separation and tip leaking [20]. In the ANSYS simulations, the waft coefficients, angles, and rotation speed were all fixed. The SST turbulence model was imposed, and so the performance of the turbine improved as the adjustable vane angle and float path vortices were increased. The efficiency gained from a guide vane angle was significant, wherein an angle of 11.8 degrees and a glide ratio of 0.21 were optimal. Separating the floats and switching the vortex profiles both increased the efficiency of the guide vane attitude exchange [21].

In fragile systems, Wells turbine converters are typically used. Stronger lift forces and separation behaviors are generated by IFS profiles due to their concave shape in the submit-mid-chord region compared to NACA profiles. CFD analysis compared six different IFS and NACA blade designs. In comparison to NACA, IFS's operating spans and torque technology improved by 24.1%, and the IFS torque was also improved. The maximum torque coefficient was also increased by VTB20IFS, by 71 percent. VTB20IFS's superior separation region was validated by SS streamline contours [22]. Using NACA 0021 constant chord blades, the tool simulated the efficiency of a Wells turbine. Turbine performance and aerodynamics were predicted using the computer model. The model's prediction of the stall glide coefficient for the turbine was spot on. To better comprehend float physics and optimize the turbine's operating range and performance, both normal and stall scenarios were investigated. Turbine stalling due to a loss of tip clearance was explained by CFD data [23]. The aerodynamic forces, compressibility, and isolated and cascade float models of the blade profiles were analyzed using a CFD model. When taking into account prior data, the NACA 0015 blade profile was used and generated the strongest aerodynamic forces. Additionally, the 15% CA9 blade was favored based on the estimated slope of the cascade force and pressure curves. Once again, 15% CA9 performed better than NACA 0015 [24]. Power generation was improved by imitating the owl's and merganser's static trailing edges. The ideal amount of static for trailing chords was between 0 and 10%. Its glide coefficient was determined using the RANS equation with the help of ANSYS-CFX Float at a simulated 15.0. The 5%C torque is improved by prolonging the SETE. Above 5%C, the working range decreased, and the stall factor got close to FC. The SETE blade made it 23.4% of the way before stopping. The effectiveness of the SETE blades drops by 5.4% due to pressure loss. In comparison to blades with strong chord duration of the same size [25], SETE generated more torque. A lumped parameter model was used to simulate the interaction between the turbine and air mass in the chamber. The compressibility of the air in the chamber is the mechanism between air volume and the turbine duct, and it created hysteresis. Differences in performance do not matter for Wells turbines because they operate at non-dimensional frequencies [26]. The onset and severity of stall are the primary focus of this analysis of the turbine's performance. Highsolidity to simulate an oscillating water column wave power conversion device, a model utilizing Wells turbines, was required. The NACA 0021-based design profile was used. Spalart–Allmaras turbulence, and k-omega and Reynolds strain turbulence models were investigated using the RANS equations as a constant. The increment in nearby torque contribution has been achieved throughout the blade floor as the blade span is increased without blade separation. The torque dropped during a stall [27]. Testing and modeling were performed on a miniature version of the Wells turbine. A REWEC rotor with a NACA 0015 profile was implemented.

Non-dimensional torque, efficiency, and pressure drop were calculated, as well as the inlet and hub-nostril form of the turbine's tip. Principal drift features were related to stagnation pressure contours on iso-helicity surfaces and meridional tangential vorticity contours [28].

Based on the observations that are obtained from the literature survey [1–36], the process of designing a Wells turbine and optimizing its performance is identified out and so depicted in Figure 1.
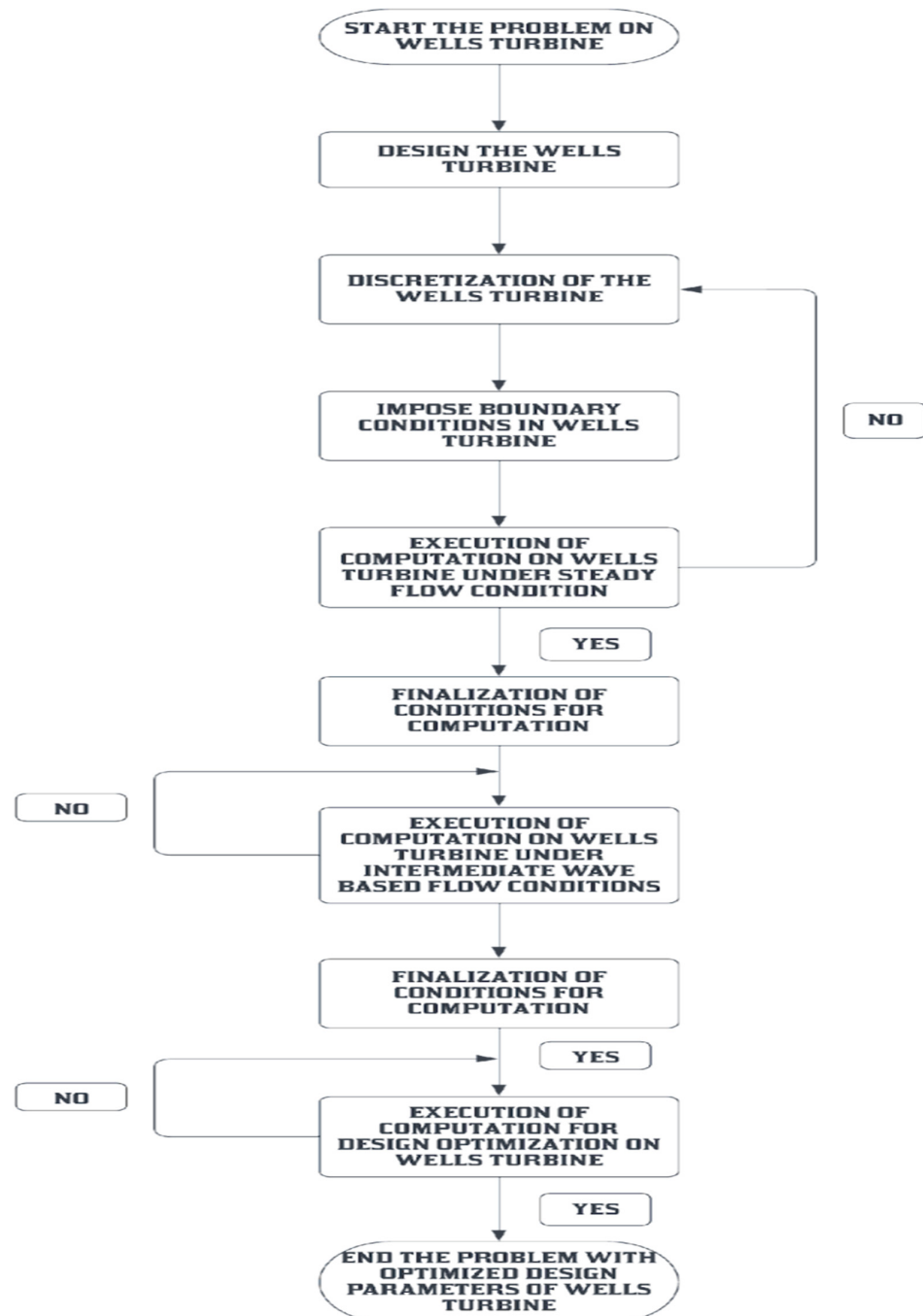
Figure 1. Work processes involved in this research.

Figure 2 represents the engineering procedures imposed in this work, which comprises CFD, computational structural, and modal analysis. CFD is used for the development hydrodynamic forces over the Wells turbine and for the estimation of torque produced by the Wells turbine. The computational structural analysis is used for the selection of suitable material that can effectively resist hydrodynamic loads and so provide a high lifetime to

the blades. The modal analysis is used for the estimation of natural frequencies of the Wells turbine and so supports the development of energy extractions through the Wells turbine. Finally, the optimized Wells turbine with a high energy extraction rate and high structural lifetime has been adopted in the energy extraction process for real-time applications.
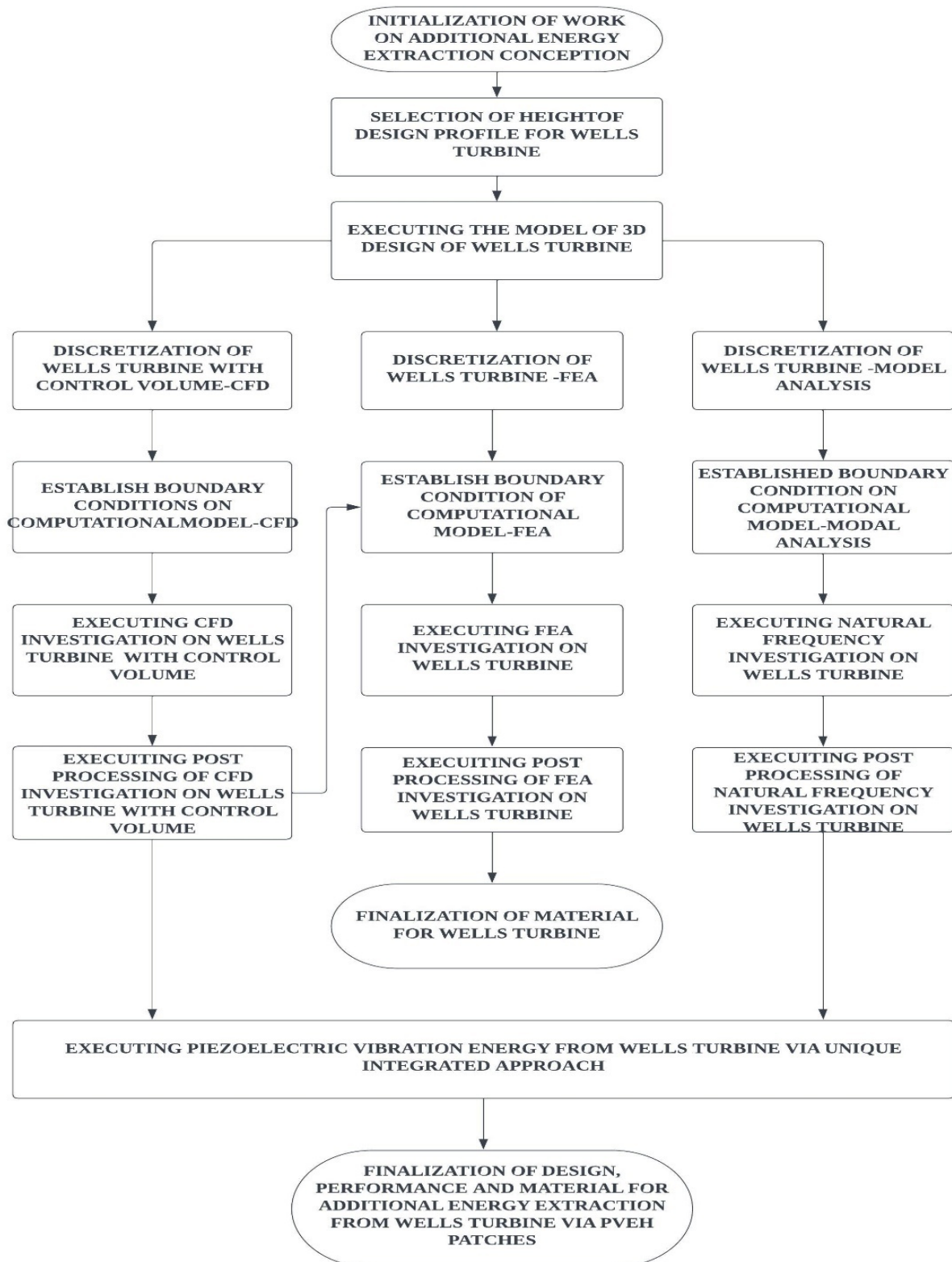
Figure 2. Work process involved.

2. Computational Methodologies

From the literature survey [1–36], it is observed that the previous works failed to impose the standard design calculations in the development of Wells turbine. Henceforth, this work is finalized to impose standard design procedures for the development of Wells turbine through the help of a bottom-up design approach. Since top-down approaches comprise assumption-based initialization, this work confirms the use of a bottom-up design approach. In a bottom-up approach, relevant design factors are chosen with previously obtained data, creating what are typically termed as historical relationships. The collected historical data and their typical relationships are revealed in Figures 3–5.
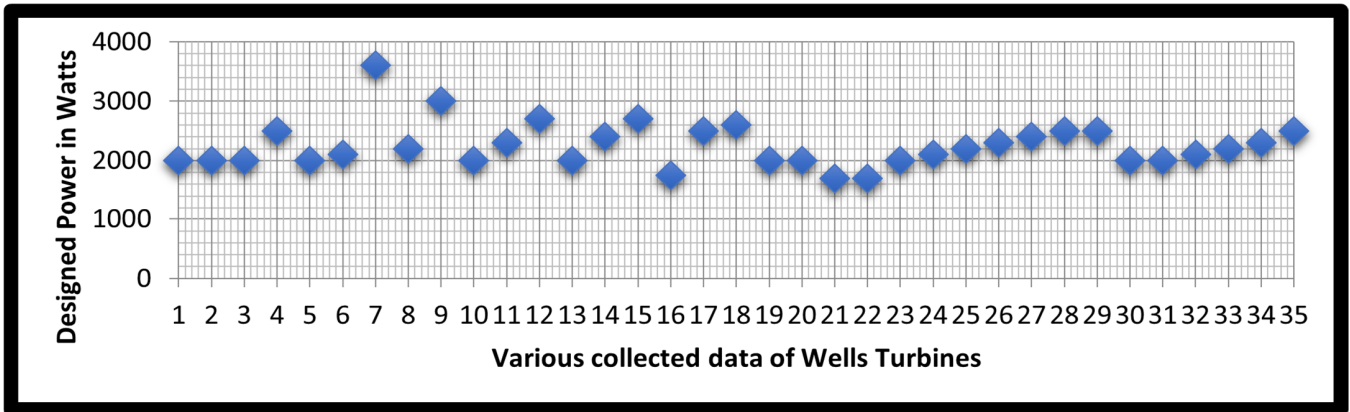
Figure 3. Various Wells turbines' data with respective power [1–36].
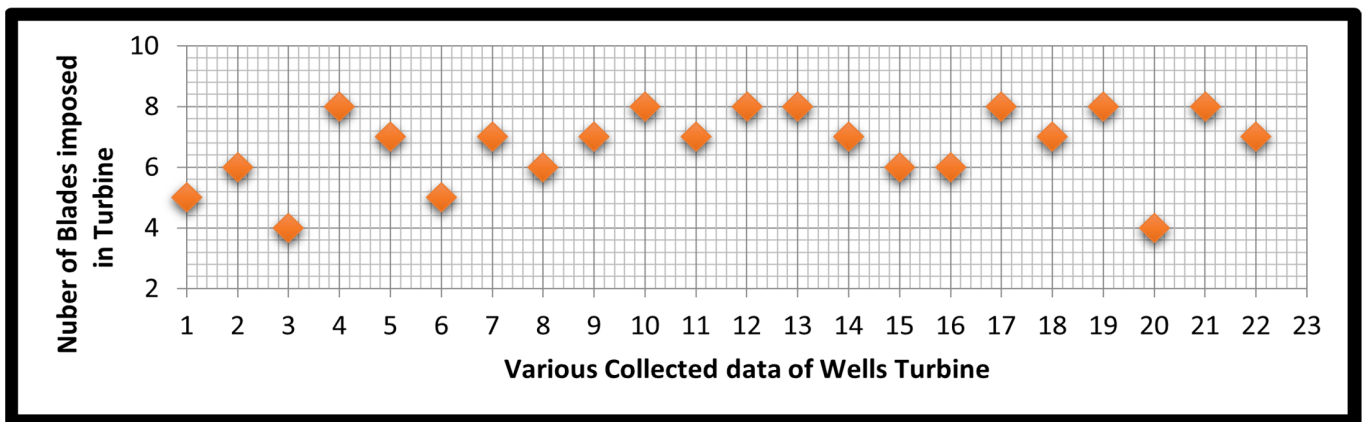
Figure 4. Various Wells turbines data with the respective number of blades [1–36].
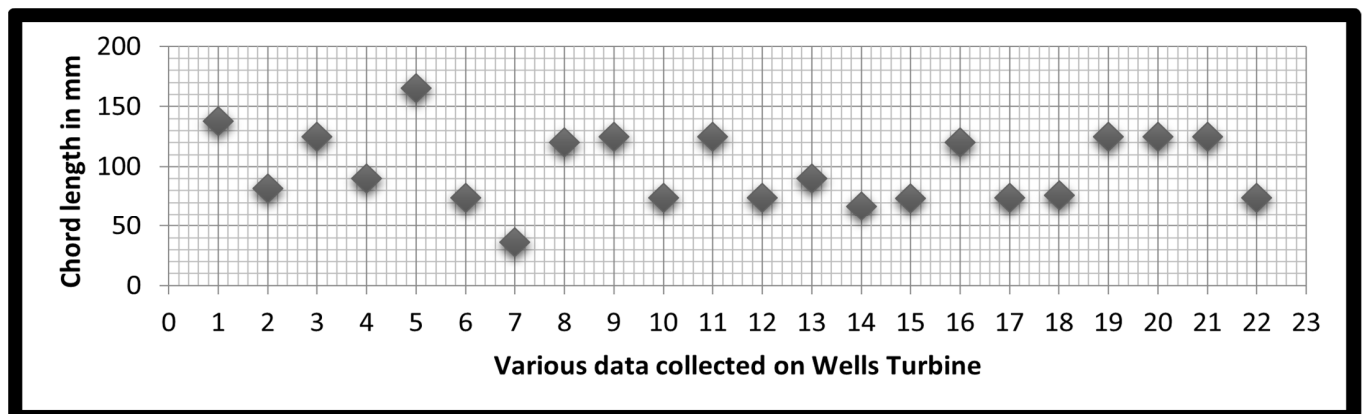
Figure 5. Various Wells turbine data with respective chord length [1–36].

2.1. Design Process

For this work, the imposed historical data and relationships concern the hydropower in watts, number of blades used, chord length in mm, and the radius of a hub to blade in mm. Figure 3 relates the various data of the Wells turbine with respective hydropower in watts, which is collected from the prior-discussed literature survey [1–36]. From Figure 3, it is observed that the maximum hydropower of 2250 W has been frequently imposed.

Figures 4 and 5 show the data of various Wells turbine with their corresponding number of blades and their chord length in mm. From Figure 4, the obtained number of blades is 7. Also, from Figure 5, the obtained chord length is 100 mm; i.e., $C_{WT}^B = 100$ mm.

$$A_{\text{Wells Turbine}} = \pi \times (r_{\text{blade}})^2 \tag{1}$$

$$\text{Circum}_{\text{Wells Turbine}} = 2\pi r_{\text{blade}} \tag{2}$$

$$\text{Circum}_{\text{Wells Turbine}} = 7 \times C_{WT}^B + 7 \times T_{WT}^B \tag{3}$$

From the shape of the conventional Wells turbine, the general relationships are derived, which are expressed in Equations (1)–(3). Equations (1)–(3) express the cross-sectional area of the Wells turbine and the circumference of the Wells turbine. To initiate the design process, the clearances between the blades play a major role. In this work, three different clearances are imposed, and so the different design data-based Wells turbines are framed. For sample calculation, the tolerance (clearance) between blades is assumed as 100 mm, and thus, $T_{WT}^B = 100$ mm.

$$\text{Circum}_{\text{blade}} = 1400 \text{ mm} \ \Rightarrow 2\pi r_{\text{blade}} = 1400 \Rightarrow r_{\text{blade}} = \frac{(1400 \times 7)}{(2 \times 22)} = 222.73 \text{ mm}$$

Additionally, another historical relationship has been organized between the hub's radius and the blade's radius. The comprehensive outcome of the recent historical relationship is revealed in Figure 6. Finally, from Figure 6, the unique relationship has been derived and is expressed in Equation (4).

$$\frac{r_{hub}}{r_{blade}} = 0.672 \tag{4}$$

$$\frac{r_{hub}}{334.1} = 0.672 \Rightarrow r_{hub} = 0.672 * 334.1 = 224.5152 \text{ mm}$$
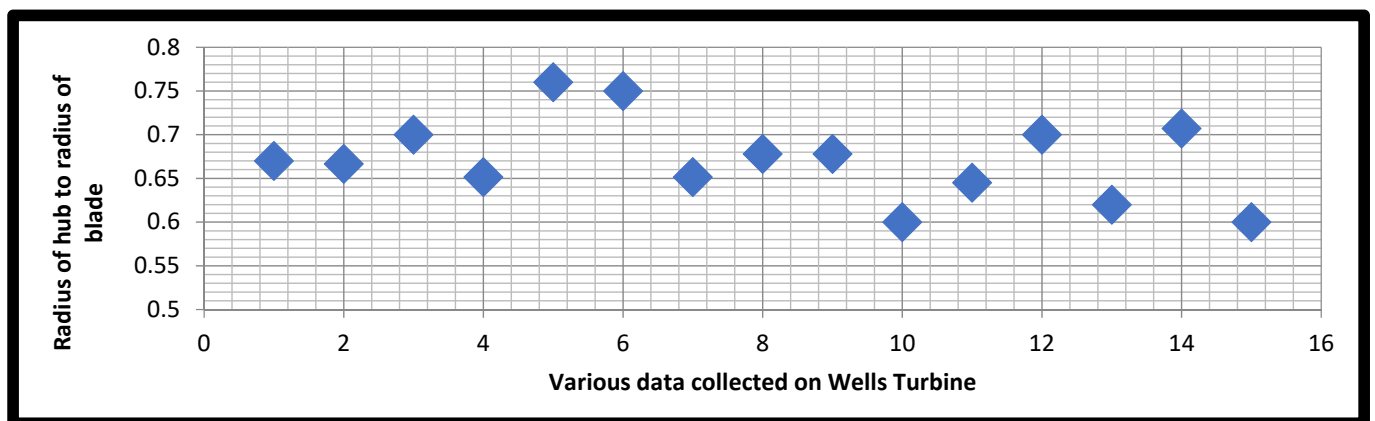

Figure 6. Various Wells turbines with respective radii of the hub to blade [1–36].

The shortlisted airfoil for this work from the literature survey [1–36] is NACA 0015. Table 1 depicts the final design data of the Wells turbine with different wingspan and main diameters in mm. Similarly, other cases are derived, and the seven cases' design data are listed in Table 2.

Table 1. Final design data of primary case.

Sl. No	Description	Value
1	Chord length	100 mm
2	Wingspan	219.1696 mm
3	Hub Diameter	449.0304 mm
4	Main Diameter	668.2 mm
5	Chosen airfoil	NACA 0015
6	Thickness for both hub and blades	15 mm (15% of the chord)
7	Number of blades	7

Table 2. Comprehensive design data of seven cases.

Design Cases	Dimensions of Various Design Factors
CASE I	Main diameter = 445.46 mm; Hub diameter = 299.35 mm; Wingspan = 146.11 mm; Tip clearance = 100 mm;
CASE II	Main diameter = 582.738 mm; Tip clearance = 100 mm
CASE III	Main diameter = 552.703 mm; Tip clearance = 150 mm
CASE IV	Main diameter = 732.036 mm; Tip clearance = 150 mm
CASE V	Main diameter = 668.2 mm; Tip clearance = 200 mm
CASE VI	Main diameter = 887.3696 mm; Tip clearance = 200 mm
CASE VII	Main diameter = 1106.5392 mm; Hub diameter = 449.0304mm; Wingspan = 438.3392 mm; Tip clearance = 200 mm

2.2. Computational Fluid Dynamics

Since this work primarily deals with the comprehensive investigations of various performance factors, an investigation based on the flexible and advanced engineering approach is mandatory for this work. Henceforth, the imposed Methodology for this work is computer-aided engineering, in which CFD provides a major contribution and also aims to determine the torque of the Wells turbine, hydrodynamic drag, hydrodynamic pressure on Wells turbine, and hydrodynamic velocities over the Wells turbine.

2.2.1. Computational Model

The Wells turbine, along with relevant control volume, is taken here as the computational model. Seven different design profiles of the Wells turbine were designed with the help of designed data. Each of the seven design profiles has a distinct hub diameter and blade length variation. The Wells turbine is designed using CATIA. The seven models have seven blades of NACA0015 airfoil with a 100 mm chord. These seven models were designed to obtain the result of maximum torque. In addition, a control volume is created around the Wells turbine. The typical fluid dynamic control volume and the Wells turbine's traces are revealed in Figure 7. For the development of control volume, the diameter of Wells turbine is picked as reference data, and so the entire volume is constructed. The rear position of the control volume is kept higher than the frontal position of the control volume. This imbalance in design data can permit the flow to settle after it impacts with Wells turbine.
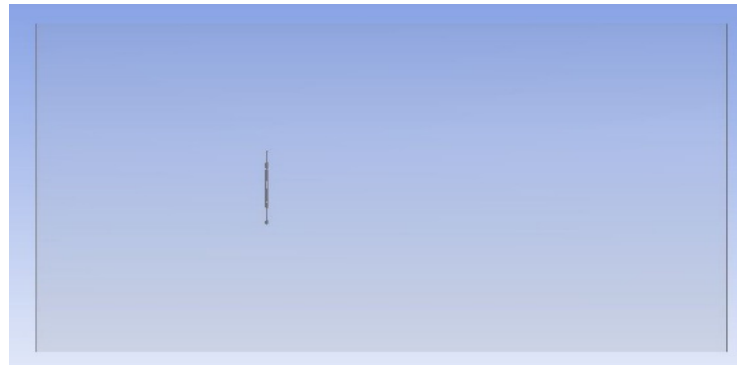
Figure 7. A systematic view of Wells turbine inside the control volume.

2.2.2. Discretization

Figure 8 represents the discretized mesh of the Wells turbine with control volume. The size function of the Wells turbine is "proximity and curvature" as the blade cross-section is of airfoil geometry. So, to captures the trailing edge in an effective manner, the above-said function is chosen. High smoothing is also chosen in addition to a fine relevance center. Table 3 provides the number of nodes and elements obtained for different mesh face sizes used for different cases of simulations that are imposed in grid independence study.
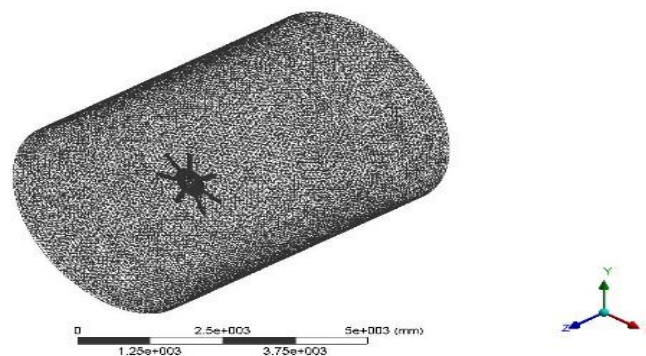
Figure 8. Discretized mesh of Wells turbine.

Table 3. Statistical data of nodes and elements for seven cases.

Various Mesh Cases	No. of Nodes	No. of Elements
CASE-1	170,185	934,788
CASE-2	196,670	1,083,869
CASE-3	157,498	865,671
CASE-4	681,382	3,889,953
CASE-5	176,180	972,195
CASE-6	238,700	1,324,759
CASE-7	693,333	3,640,060

2.2.3. Boundary Conditions

In this analysis, four inlet velocities are used such as average steady state velocity of water, shallow water velocity, wave celerity velocity, and the maximum wave velocity. The pressure outlet is zero for all the inlet velocities, and the operating pressure is 103,125 Pa. No slip condition is applied on the Wells turbine because of the friction. Instead, specified shear is applied on the wall. Four inlet velocities are the average velocity of water, shallow water velocity, intermediate water velocity, and deep water velocity. Average water velocity is obtained using surface water velocity estimated as 0.4 m/s through Equation (5) and the correction factor estimated as 0.85.

$$\text{Average velocity of water} = 0.4 \times 0.85 \Rightarrow 0.34 \ \text{m/s} \tag{5}$$

$$\text{Shallow water velocity} = \sqrt{g \times \frac{\lambda}{20}} \Rightarrow \sqrt{g \times \frac{96.78}{20}} \Rightarrow 1.54 \ \text{m/s} \tag{6}$$

The shallow water velocity is estimated as 1.54 m/s with the help of Equation (6),in which the imposed hydro-fluid properties density, dynamic viscosity, and kinematic viscosity are used. The values of these properties are 1030 kg/m^3, 1.793×10^{-3} kg/m-s, and 1.787×10^{-6} m^2 s^1.

2.2.4. Solver Data and Governing Equations

This study uses a pressure-based solver because of incompressible flow and constant density. The turbulence models used are Spalart–Allmaras and k-epsilon with enhanced wall treatment. The relevant shortlisted turbulence model is further imposed in all the models that give the best out-turn for boundary layers to acquire an adverse pressure gradient. Steady-state analysis is taken over for all seven cases. The turbulent viscosity ratio is fixed as 10% because of the high density of the imposed fluid. Concerning the new technology for renewable energy, the solver has to be setup with governing equations that are obtained from CFD fundamental concepts [37–39]. The RANS equations are certain to solve real problems using computational strategy, time continuity, and momentum relationships. The coupled algorithm-based pressure and velocity coupling has been implemented with higher-order approximations.

2.3. Computational Structural Analyses

In this part of the work, a structural analysis is carried out using the boundary conditions that will be discussed further down to determine the total deformation, equivalent stress, equivalent elastic strain, stress intensity, strain energy, shear stress, and normal stress for materials such as carbon fiber-reinforced polymer (CFRP) materials, glass fiber-reinforced polymer (GFRP) materials, and relevant lightweight alloys. This computational structural analysis aims to determine a suitable lightweight material for the Wells turbine that results in less deformation, stress, and strain with high lifetime.

The Wells turbine with the composition of seven blades is employed as a computational model for this structural analysis. This turbine is designed to obtain the maximum efficiency to extract the energy from ocean waves with the high-power design profile of NACA 0015. Figure 9 shows the computational model of a seven-bladed Wells turbine. The discretization is the next phase that is involved in this computational structural analysis. The discretized mesh of the computational model used in this investigation is seen in Figure 10. The "proximity and curvature" size function is implemented in this work, and the size function can be perfectly captures the Well turbine curvatures. In addition, high smoothing is selected, while a coarse relevant center is selected. Since all the seven cases are different in terms of design data, the meshed elements are obviously different for all the seven cases. For the sake of example, the statistical reports of case IV and case VI are provided that further enhance the reliability of this work. The total number of nodes and elements in case IV is 572,774, while the total number in case VI is 918,984.

In this study, the computational structural analysis has been computed with the help of a one-way coupling-based fluid–structure interaction approach. For hydrodynamic loading extraction purposes, two different inlet velocities are used for two different cases. One is the surface velocity of water, which is 0.34 m/s, and the second is deep water velocity, which is 23 m/s. The support used in this work is fixed support that is provided in all the interactions between the hub and blades of the Wells turbine. The material properties of the imposed lightweight materials have been extracted from the literature survey [40,41] and engineering data library from the imposed computational tool, i.e., ANSYS Workbench 17.2. The governing equations imposed in this work used are from force-and-displacement-based relationships, and stress-and-strain-based relationships [40,41]. For this analysis,

each blade can be treated as a cantilever beam because of the production of fixed support to the hub. The uniformly distributed loads are imported from hydrodynamic pressure obtained through steady fluid flow analysis.
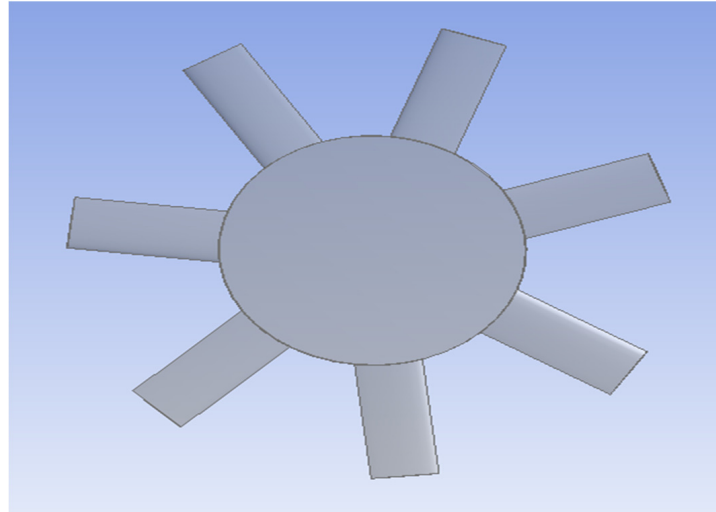

Figure 9. Typical representation of the computational model for structural analysis.
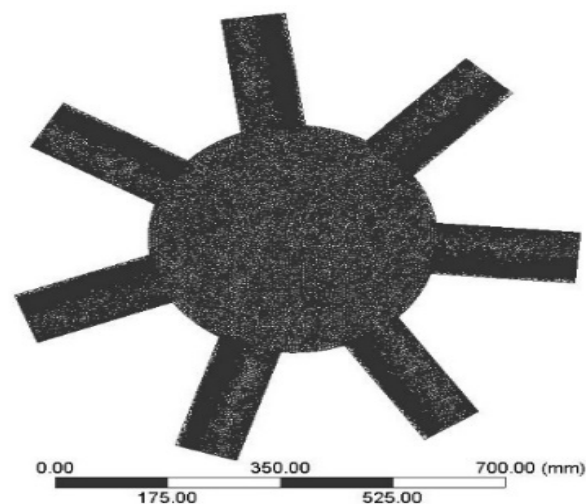
Figure 10. Discretized structure of Wells turbine.

2.4. Computational Analysis for PVEH

The Wells turbine, which has seven blades, can be disassembled into its component parts. To begin, the model is held in a stationary position while it is being supported. After that, there is no restriction on how it vibrates. The frequency of the required material is then determined via modal analysis, and this information is then employed in the power of piezoelectric vibrational energy harvester (PVEH) calculations. Figure 9 is a front-view illustration of a common computer model that is utilized in the process of vibrational analysis. The discretized structure of the Wells turbine is shown in Figure 10. The boundary condition that must be complied with is illustrated in Figure 11. For this modal analysis, the discretization has been executed, and the details are as follows: the number of nodes is 88,975, and the number of elements is 53,859. Also, the size function used in this computational vibrational analysis is curvature, and this smoothing is high.
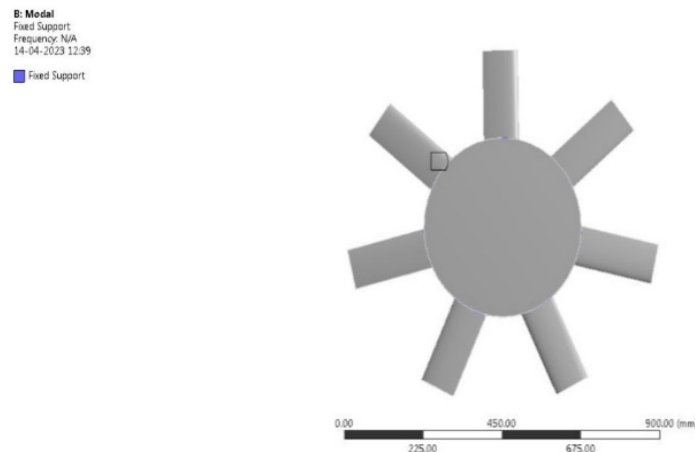
Figure 11. A typical isometric view-based representation of imposed boundary conditions on the Wells turbine (WT).

The inherent resonance frequencies and mode forms of a structure should be identified. A linear dynamical analysis is the process of studying modes. Since the overall acceleration, velocity, and location of the structure at each site are constantly unknown, the dynamic response of a structure must be calculated by first solving the fundamental equation of motion. Control of this system is defined by Equation (7) [42–47].

$$[m_{WT}]\left\{\frac{d^2u}{dx^2}\right\} + [C_{WT}]\left\{\frac{du}{dx}\right\} + [K_{WT}]\{u\} = \left\{F(t)_{Hydrodynamic}\right\} \tag{7}$$

Since the resonance frequency and mode forms are independent of the external load, they must be set to zero for modal analysis. However, the morphologies of natural frequencies and modes can only be expressed using complex numbers; therefore, damping effects are currently being disregarded. As seen in Equation (8), this first optimized governing equation is for modal simulation.

$$[m_{WT}]\left\{\frac{d^2u}{dx^2}\right\} + [K_{WT}]\{u\} = 0 \tag{8}$$

From the perspective of time domain dynamics, this problem can be thought of as a body either at rest or moving at a constant pace. Therefore, $\left\{\frac{d^2u}{dx^2}\right\}(t) = 0$; Equation (9), a condensed version of the governing equation, governs the modal computation.

$$[K_{WT}]\{u\} = 0 \tag{9}$$

2.4.1. Experimental Validation—1

A thorough investigation of experimental analysis is conducted to ascertain the efficacy of computational work. The MIDE quick pack QP 10W is utilized in the experimental configuration the authors suggested. A total of 2.5 mW of power was retrieved for this study. Therefore, in order to confirm the computational work and compare the experimental setup, a three-dimensional model of the experimental setup is produced with the assistance of CATIA, and then, it is analyzed in ANSYS Workbench 17.2. The authors suggest the boundary conditions and material characteristics. A modal analysis is then performed after the CFD simulation to ascertain the frequency of the relevant material. Figures 12 and 13 [42–47] vividly illustrate the well-established research of aerodynamic and modal analyses.
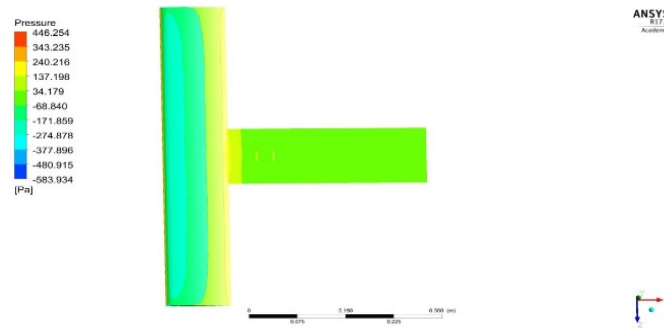
Figure 12. Pressure distribution on the proposed experimental setup.
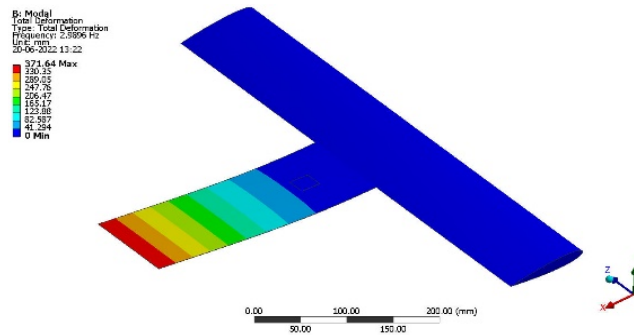
Figure 13. Total deformation on the experimental setup.

A computational simulation is used to determine the required values for the calculation. Quick pack QP 10W is used as a calculation sample. Equations (10) and (11) substitute the expected computational result-based data. The pressure on the piezoelectric patch is 34.179 N/m^2.

$$P_{\text{Intermediate}}^{\text{Validation}} = d_{\text{lwm}}^2 w^2 f^2 \times \frac{18 \times T_{\text{PL}}}{\left[(W_P) \times (L_{\text{PL}})^2 \times ([t_P] + [T_{\text{PL}}])^4 \right]} \times \frac{\rho_{\text{lwm}}}{[1 + f \times \varepsilon \times (\rho_{\text{lwm}})]} \tag{10}$$

$$P_{\text{Final}}^{\text{Validation}} = \left(P_{\text{Intermediate}}^{\text{Validation}} \right) \left(\frac{(0.44 * L)^5}{36} - \frac{L(0.44 \times L)^4}{6} + \frac{5L^2(0.44 \times L)^3}{12} - \frac{L^3(0.44 \times L)^2}{2} + \frac{L^4(0.44 \times L)}{4} \right) \tag{11}$$

Inputting the appropriate values into the equation yields an estimated power of 2.3 mW. Therefore, compared to experimental work, computational analysis error was 8%, which lies within the acceptable range. Table 4 contains a complete set of trial results and suggested data of this work. It is evident from Table 4 that the error percentage is within the allowed range, indicating that the PVEH patches can be used to extract electrical energy using the mathematical and analytical approach that is being presented for this work. With this imposed integrated strategy now verified, the authors are prepared to apply it to further real-time use cases. But first, nature-inspired Wells turbine uses the same methodology.

Table 4. Experimental and computational studies verify the legitimacy of electrical power extractions [42–47].

The Developed Electrical Power (mW) as Measured in Experimental Settings	The Resulting Electrical Power (in mW) from the Method Proposed Here	Error Percentage
2.5	2.3	8

2.4.2. Experimental Validation—2

In order to improve the reliability of the required procedure, a second research is required after the first one has confirmed the accuracy of the results of the energy extraction. This part is devoted to a validation study [42–47] because of the significance of the method that was implemented in this part of work. A separate and easier-to-understand validation design, which can be shown in Figure 14, has been developed. Figure 15 depicts the results of applying the models. Using ANSYS Fluent, we were able to come up with an estimate for the required pressure variation on the base model. Figure 16 illustrates the ultimate effect that the vibrations of the base object had.
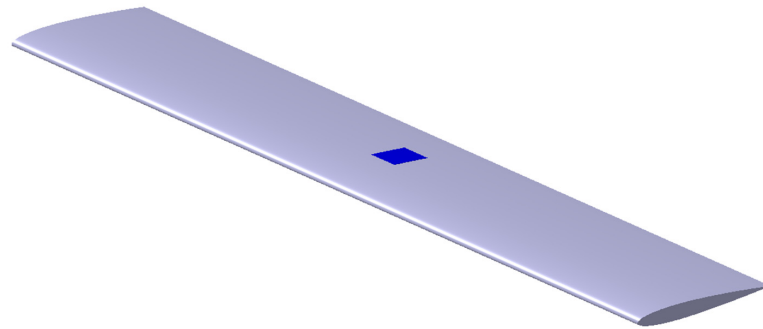
Figure 14. The typical isometric representations of secondly modified base model along with PVEH patches.
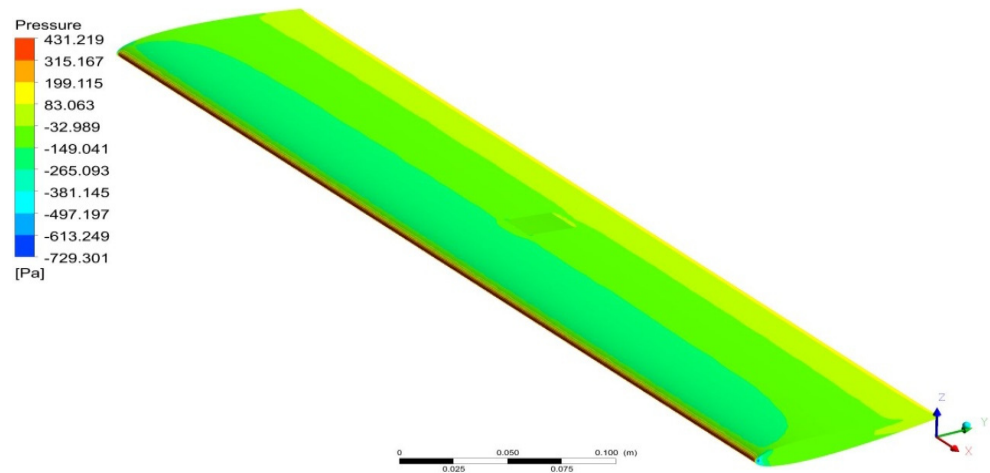
Figure 15. The typical isometric representations of pressure loads acting on the secondly modified base model along with PVEH patches.
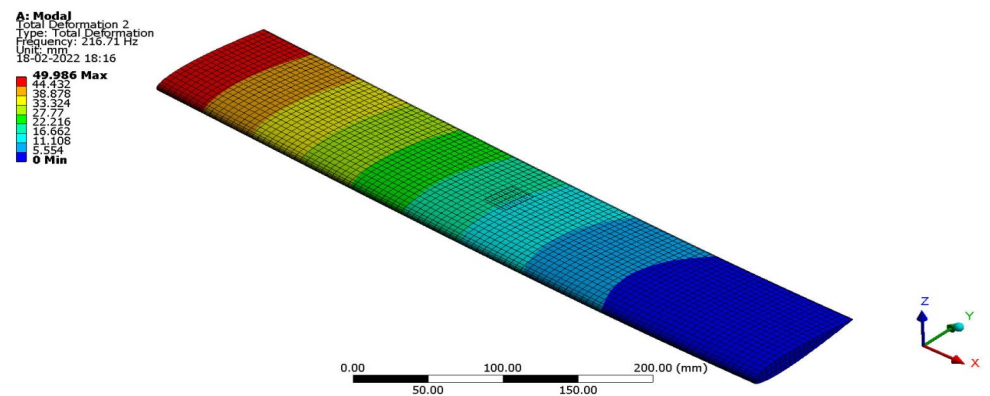
Figure 16. The typical isometric representations of freely vibrated structure of secondly modified base model along with PVEH patches.

Similarly to the first experimental validation test, the second experimental test is also conducted, and so the outcomes are listed in Table 5.

Table 5. Validation of electrical power extractions through experimental and computational outcomes [42–47].

The Developed Electrical Power (mW) as Measured in Experimental Settings	The Resulting Electrical Power (in mW) from the Method Proposed Here	Error PERCENTAGE
2.5	2.58	3.1

From Tables 4 and 5, it is clearly observed that the imposed energy extraction approach based on advanced computational method is reliable and suitable to impose in real-time applications. Also, it is learned that the additional approaches such as CFD and computational structural analysis are also validated with these experimental validations.

3. Results and Discussion

Firstly, the optimized Wells turbine is obtained with the help of CFD analysis for all seven cases with four different inlet velocities, such as 0.34 m/s, 1.54 m/s, 12.10 m/s, and 23 m/s. Secondly, the computational structural analysis is taken for the optimized Wells turbine using various lightweight materials.

3.1. CFD Outcomes

In CFD, the primarily focused outcomes have been finalized as torque and hydrodynamic drag; the secondary focused outcomes are hydrodynamic pressure acting on the Wells turbine and hydrodynamic velocity variations in and over the same Wells turbine.

3.1.1. Results and Discussion on Design Data-Based Modified Cases

Firstly, the CFD investigations are computed on first case of the Wells turbine. Figures 17–20 depict the hydrodynamic velocity and pressure variations that are acting in and over the first case of the Wells turbine for the inlet velocities of 0.34 m/s, 1.54 m/s, 12.10 m/s, and 23 m/s. The outcomes are compared, and so the comprehensive studies are carried out. Based on the integrative effect among the four inlet velocity outcomes, the velocity of 0.34 m/s performance is better than the others.
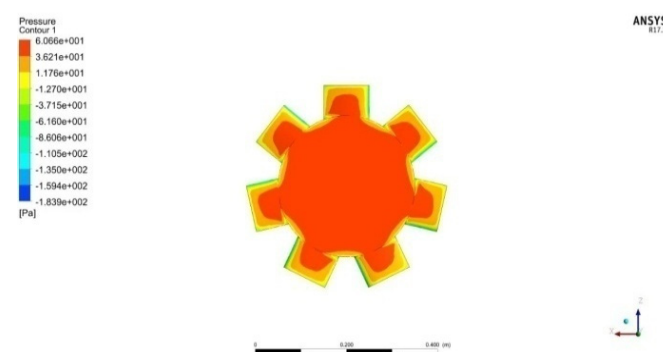
Figure 17. Pressure on first case based WT under hydrodynamic condition of 0.34 m/s.

Secondly, the CFD investigations are computed on the second case of the Wells turbine. Figures 21–24 depict the hydrodynamic velocity and pressure variations that are acting in and over the second case of the Wells turbine for the inlet velocities of 0.34 m/s, 1.54 m/s, 12.10 m/s, and 23 m/s. The outcomes are compared, and so the comprehensive studies are carried out. Based on the integrative effect among the four inlet velocity outcomes, the velocity of 23 m/s performance is better than the others.
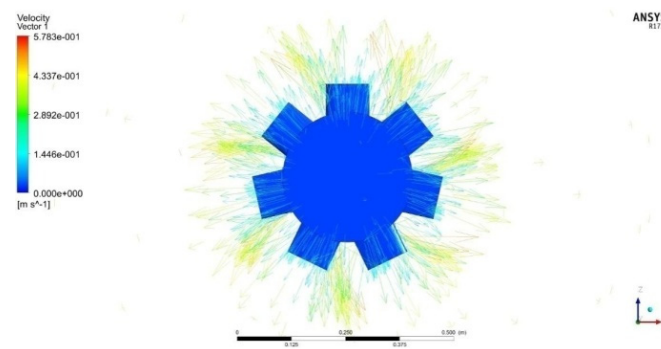
Figure 18. Hydrodynamic velocity on first case based Wells turbine—0.34 m/s speed– case-1.
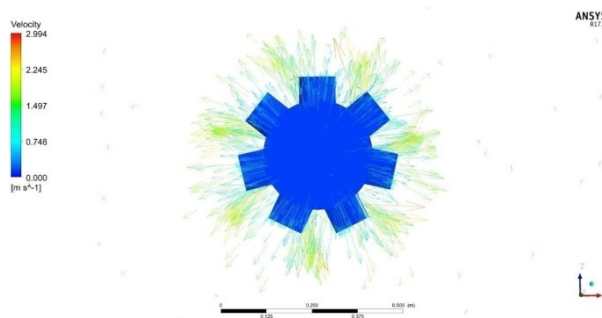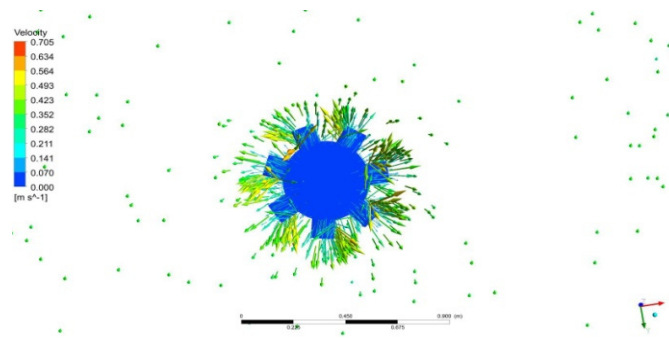

Figure 19. Hydrodynamic velocity on first case based Wells turbine—1.54 m/s speed.
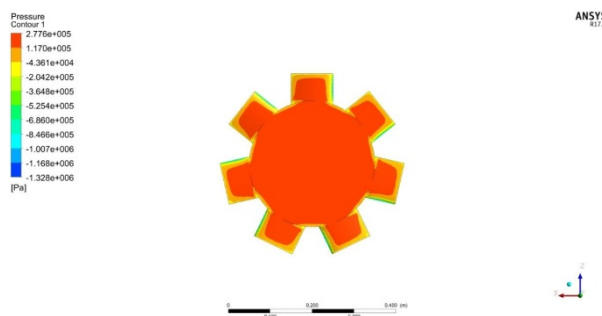
Figure 20. Pressure on first case based WT under hydrodynamic condition of 23 m/s.
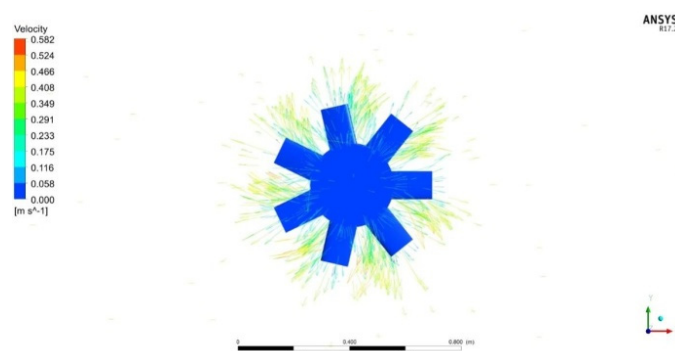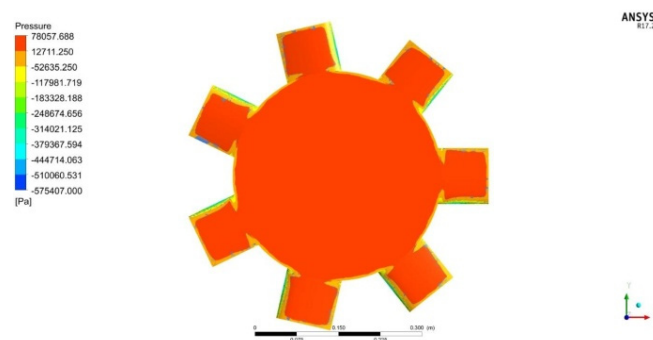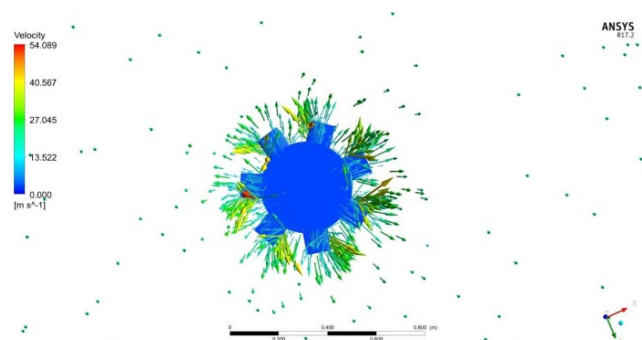

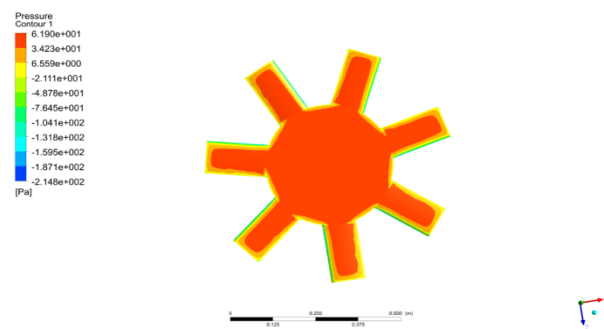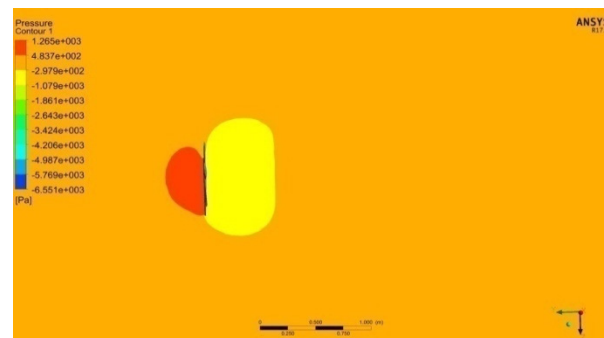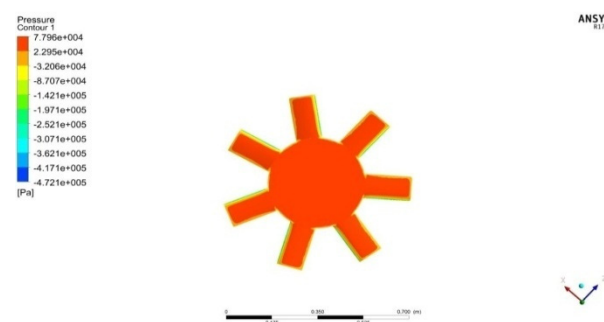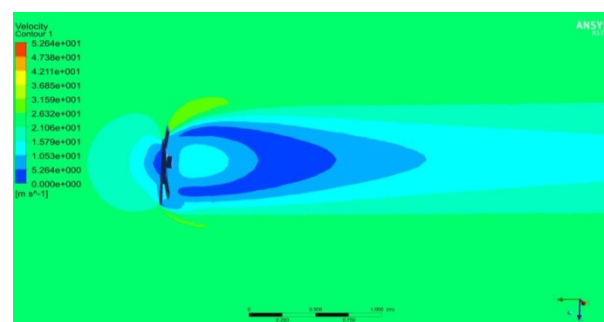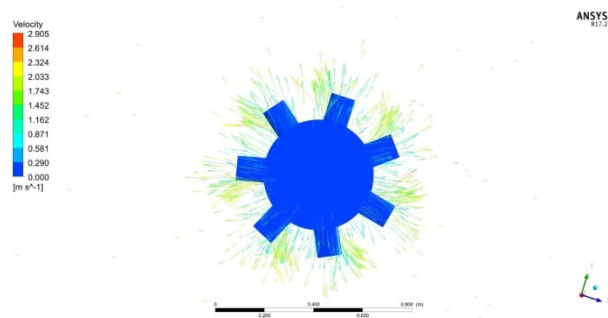**Figure 21.** Hydrodynamic velocity on second case based Wells turbine—0.34 m/s speed.
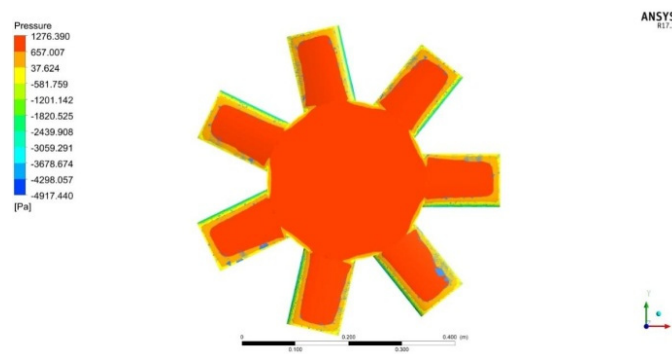
Figure 22. Pressure on second case based WT under hydrodynamic condition of 1.54 m/s.
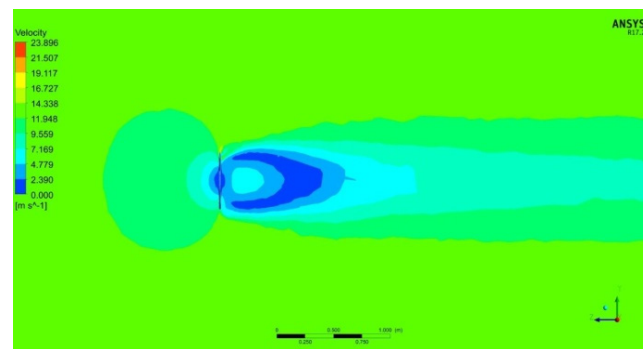
Figure 23. Hydrodynamic velocity on second case based Wells turbine—12.10 m/s speed.
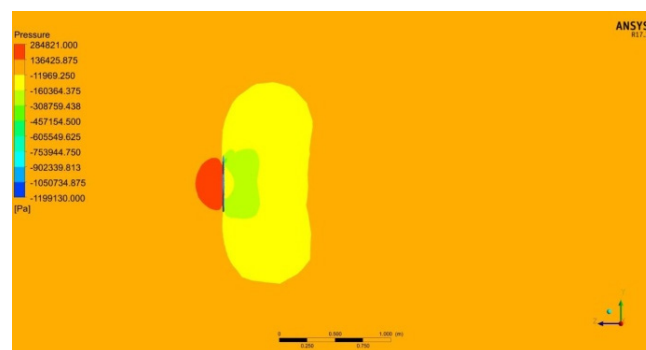
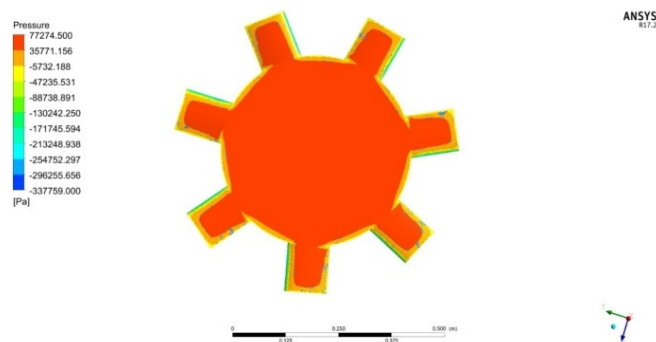**Figure 24.** Pressure on second case based WT under hydrodynamic condition of 23 m/s.

Thirdly, the CFD investigations are computed on third case of the Wells turbine. Figures 25–28 depict the hydrodynamic velocity and pressure variations that are acting in and over the third case of the Wells turbine for the inlet velocities of 0.34 m/s, 1.54 m/s, 12.10 m/s, and 23 m/s. The outcomes are compared and so the comprehensive studies are carried out. Based on the integrative effect among the four inlet velocity outcomes, the velocity of 0.34 m/s performance is better than the others.

Fourthly, the CFD investigations are computed on the fourth case of the Wells turbine. Figures 29–32 depict the hydrodynamic velocity and pressure variations that are acting in and over the fourth case of the Wells turbine for the inlet velocities of 0.34 m/s, 1.54 m/s, 12.10 m/s, and 23 m/s, respectively. The other performance factors such as hydrodynamic forces acting on the Wells turbine and torque produced by the Wells turbine are also estimated through function calculator facility.

Figure 25. Hydrodynamic velocity on third case based Wells turbine—0.34 m/s speed.
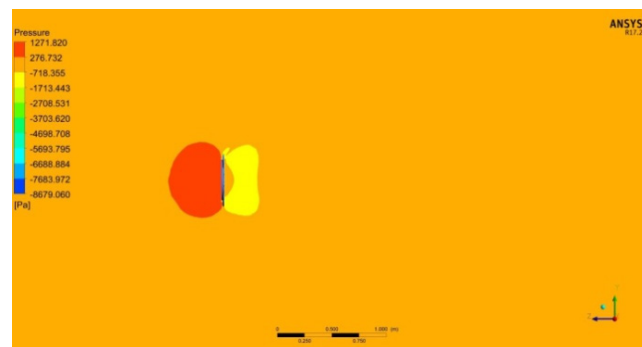
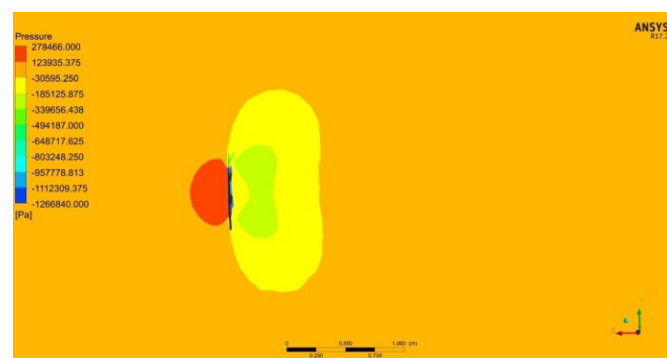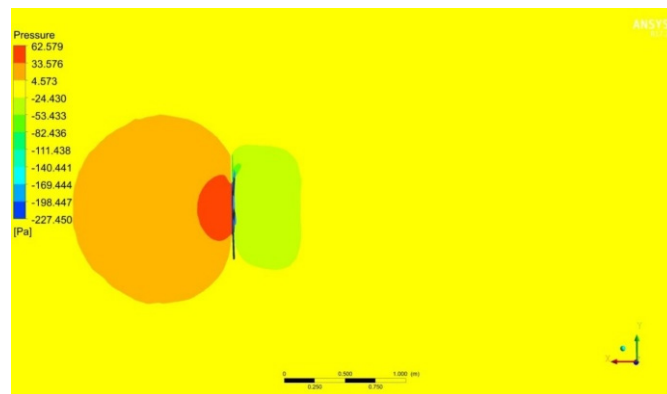**Figure 26.** Pressure on third case based WT under hydrodynamic condition of 1.54 m/s.

**Figure 27.** Pressure on third case based WT under hydrodynamic condition of 12.10 m/s.

Figure 28. Hydrodynamic velocity on third case based Wells turbine—23 m/s speed.

Figure 29. Pressure on fourth case based WT under hydrodynamic condition of 0.34 m/s.

Figure 30. Pressure on fourth case based WT under hydrodynamic condition of 1.54 m/s.

Figure 31. Pressure on fourth case based WT under hydrodynamic condition of 12.10 m/s.

Figure 32. Hydrodynamic velocity on fourth case based Wells turbine—23 m/s speed.

Fifthly, the CFD investigations are computed on the fifth case of the Wells turbine. Figures 33–36 depict the hydrodynamic velocity and pressure variations that are acting in and over the fifth case of the Wells turbine for the inlet velocities of 0.34 m/s, 1.54 m/s, 12.10 m/s, and 23 m/s, respectively. As similar as other cases, the performance factors are also determined for this fifth model.
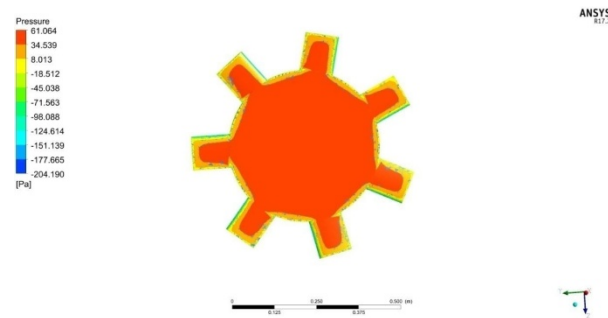
Figure 33. Pressure on fifth case based WT under hydrodynamic condition of 0.34 m/s.

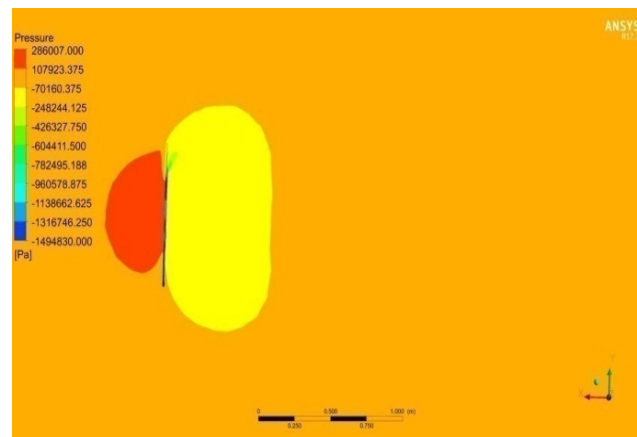**Figure 34.** Hydrodynamic velocity on fifth case based Wells turbine—1.54 m/s speed.

Figure 35. Pressure on fifth case based WT under hydrodynamic condition of 12.10 m/s.

Figure 36. Pressure on fifth case based WT under hydrodynamic condition of 23 m/s.

Sixthly, the CFD investigations are computed on sixth case of the Wells turbine. Figures 37–40 depict the hydrodynamic velocity and pressure variations that are acting in and over the sixth case of the Wells turbine for the inlet velocities of 0.34 m/s, 1.54 m/s, 12.10 m/s, and 23 m/s. The outcomes are compared, and so the comprehensive studies are carried out. Based on the integrative effect, the 0.34 m/s inlet velocity result is the most effective of the four possible inlet velocities.
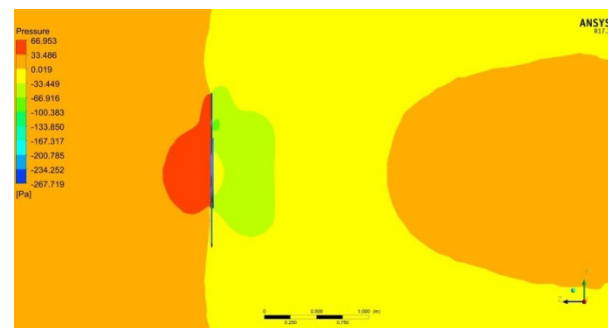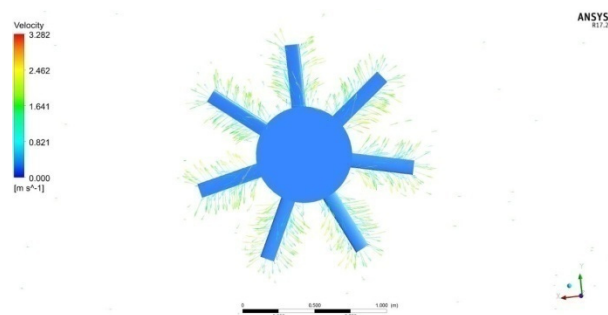
Figure 37. Pressure on sixth case based WT under hydrodynamic condition of 0.34 m/s.
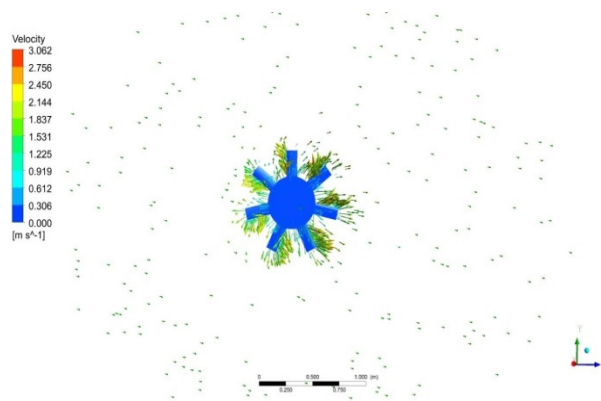
Figure 38. Hydrodynamic velocity on sixth case based Wells turbine—1.54 m/s speed.
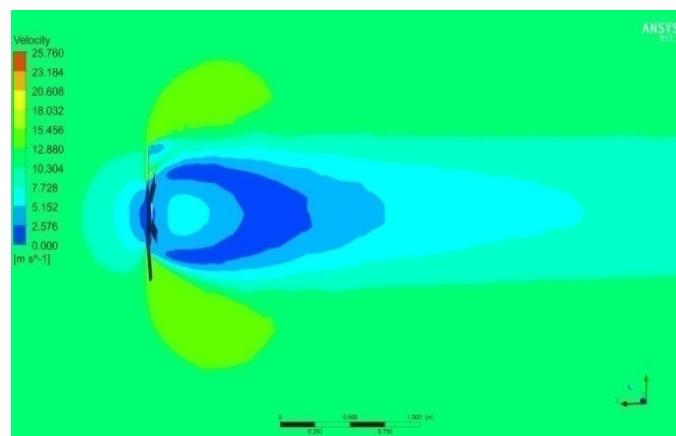
Figure 39. Hydrodynamic velocity on sixth case based Wells turbine—12.10 m/s speed.

Seventhly, the CFD investigations are computed on seventh case of the Wells turbine. Figures 41–44 depict the hydrodynamic velocity and pressure variations that are acting in and over the seventh case of the Wells turbine for the inlet velocities of 0.34 m/s, 1.54 m/s, 12.10 m/s, and 23 m/s. The outcomes are compared, and so the comprehensive studies are carried out. Based on the integrative effect, the performance of the 0.34 m/s inlet velocity is superior to the other four possible outcomes.

Figure 40. Pressure on sixth case based WT under hydrodynamic condition of 23 m/s.

Figure 41. Pressure on seventh case based WT under hydrodynamic condition of 0.34 m/s.

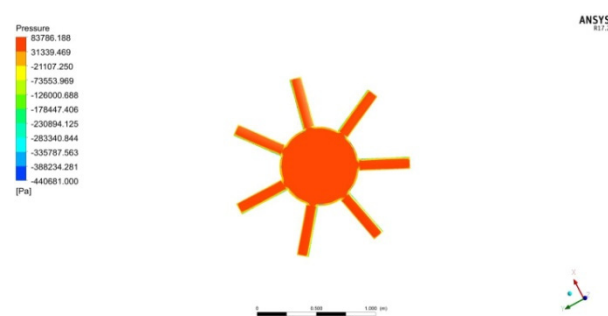**Figure 42.** Hydrodynamic velocity on seventh case based Wells turbine—1.54 m/s speed.

Figure 43. Pressure on seventh case based WT under hydrodynamic condition of 12.10 m/s.
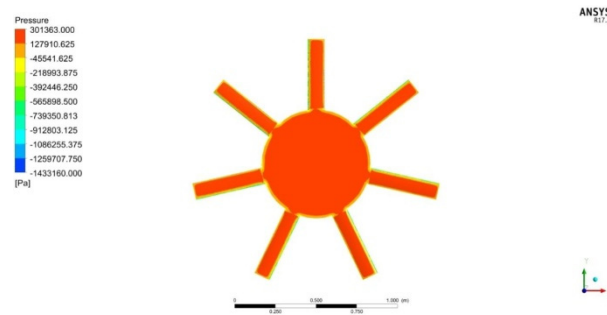
Figure 44. Pressure on seventh case based Wells turbine under hydrodynamic condition of 23 m/s.

Finally, the comprehensive outcomes of all four cases are listed in Tables 6–8. Table 6 comprises data on aerodynamic forces-based outcomes, Table 7 comprises comprehensive data on torque, and Table 8 comprises comprehensive data on power extraction.

Table 6. Torque for various imposed Wells turbine cases.

Velocity (m/s)	Torque (Nm)						
	Case 1	Case 2	Case 3	Case 4	Case 5	Case 6	Case 7
0.34	0.055215	0.154057	0.142265	0.246834	0.158302	0.418652	1.27369
1.54	1.49314	3.73196	3.9291	6.83129	3.84614	10.0088	30.0695
12.10	103.202	243.903	260.64	471.9	251.783	656.869	1919.9
23	380.127	884.07	957.654	1279.2	925.113	2393.45	6713.63

Table 7. Drag force for various imposed Wells turbine cases.

Velocity (m/s)	Drag (N)						
	Case 1	Case 2	Case 3	Case 4	Case 5	Case 6	Case 7
0.34	9.09072	13.4306	13.2765	18.8315	19.0282	26.3446	59.7228
1.54	185.191	272.619	271.242	383.472	388.983	537.146	1219.24
12.10	11,454.7	16,795.5	16,702.1	23,630.1	24,011	33,159.2	73,799.7
23	40,891.8	59,962.9	58,965.2	82,569.6	81,523.9	113,105	245,682

Table 8. Power for various imposed Wells turbine cases.

Velocity (m/s)	Power (W)						
	Case 1	Case 2	Case 3	Case 4	Case 5	Case 6	Case 7
0.34	0.143368	0.30774	0.362951	0.417528	0.28004	0.581275	1.540195
1.54	20.07226	37.19742	44.78828	60.95917	33.44393	69.07728	178.3818
12.10	11,463.88	20,004.22	26,920.69	35,328.13	18,015.37	38,139.29	92,229.6
23	81,805.03	134,024.3	98,913.09	183,986.5	127,204.8	263,356.2	594,207.1

The high power extraction rate and low hydrodynamic drag force are the predominant selection factors involved in this work. From CFD outcomes, the torque and drag forces are calculated, and they are listed in Tables 6–8. From Tables 6–8, based on integrative effect, the reasonable drag developer with torque producer-based design model is shortlisted for further investigation. From the outcomes listed in Tables 6–8, it is clearly observed that in case-4,there is better extraction of a high amount of energy from the hydro-fluid sources and also less drag produced than in other enhanced cases. Based on the integrative effect, this decision has been made, and so case-4 is finalized as the best performer.

3.1.2. Results and Discussion on Design Profile Modified Cases

Because of the high imposition of modernization, the hydro-fluid source is reducing drastically. Thus, the authors finalized further design profile modifications on case-4. Three more additional design profile modifications are imposed on the case-4-based Wells turbine. The typical representations of all three profile-enhanced Wells turbines are revealed in Figures 45–47.

In three advanced cases, two cases belong to stepped-back airfoil-based modified design profiles, and one case belongs to a zigzagged airfoil-based modified design profile. As per the aforesaid same boundary conditions and control volume dimensions, the computational investigations are computed. The typical hydrodynamic velocity variations in and over of all three advanced cases are revealed in Figures 48–50. Additionally, to obtain a further view about the turbulence development and its effect that supports the development of high hydropower, studies on turbulence behavior are also executed. The major outcomes of the turbulence prediction such as turbulence dissipation rate and turbulence kinetic energy are determined. The variations in turbulence dissipation rate and turbulence kinetic energy in and over the Wells turbine are systematically revealed in Figures 51–56.
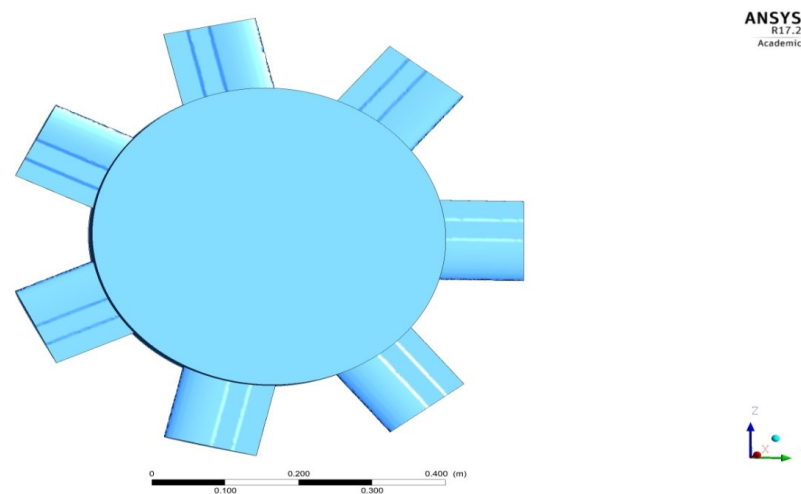
Figure 45. A typical frontal view-based representation of first stepped-back airfoil-based Wells turbine (advanced case-1).
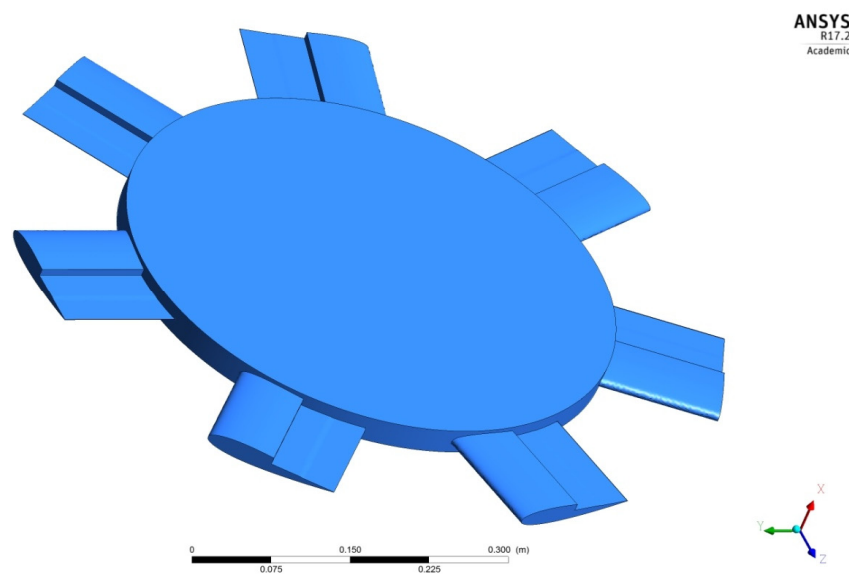
Figure 46. A typical frontal view-based representation of second stepped-back airfoil-based Wells turbine (advanced case-2).
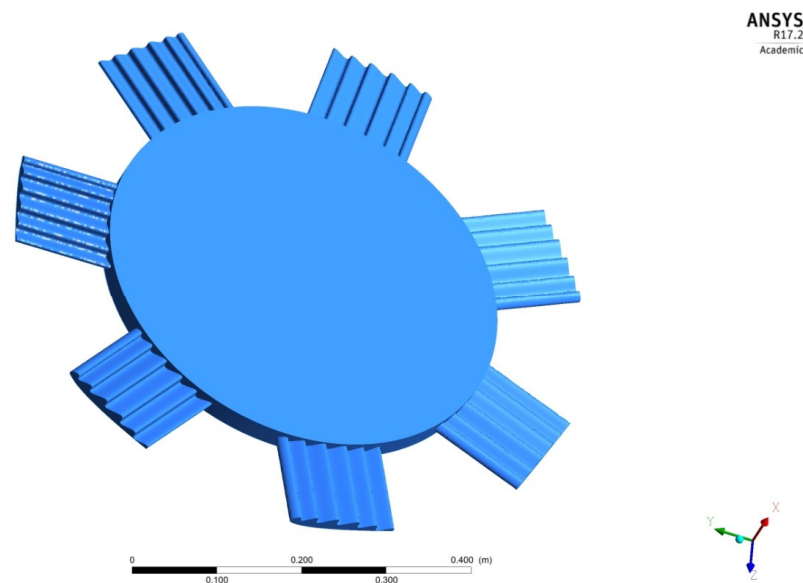
Figure 47. A typical frontal view-based representation of third zigzagged-cum-stepped-back airfoil-based Wells turbine (advanced Case-3).

After the successful completions of computations on all three additional advanced cases, the torques are captured and listed in Table 8.

From Table 9, it is clearly understood that advanced case-2 is capable of enhancing the hydro-power by 15.19 percent as compared to the conventional case-4.

Table 9. Comprehensive hydro-power outcomes of all the three advanced cases.

Number of Special Cases	Description of Special Cases	Torque (Nm)	Observations
Base	Case-IV normal cases	1279.2341	Not applicable
Case-1	Step-1	172.946	Torque is decreased by the percentage of 86.48
Case-2	Step-2	1473.54	Torque is increased by the percentage of 15.19
Case-3	Serration at top-up approach	1137.64	Torque is decreased by the percentage of 11.07
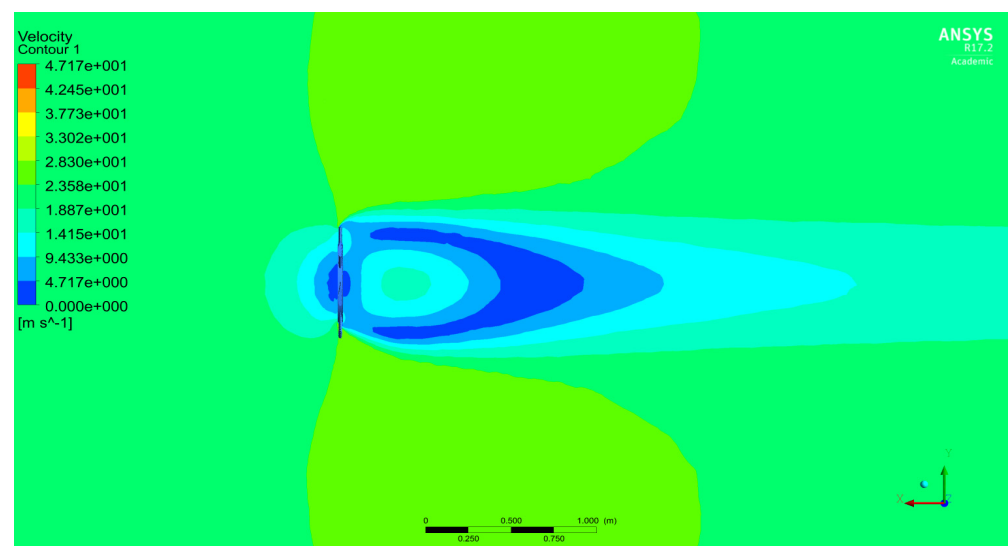
Figure 48. Hydrodynamic velocity variations in and over the Case-3-based Wells turbine.
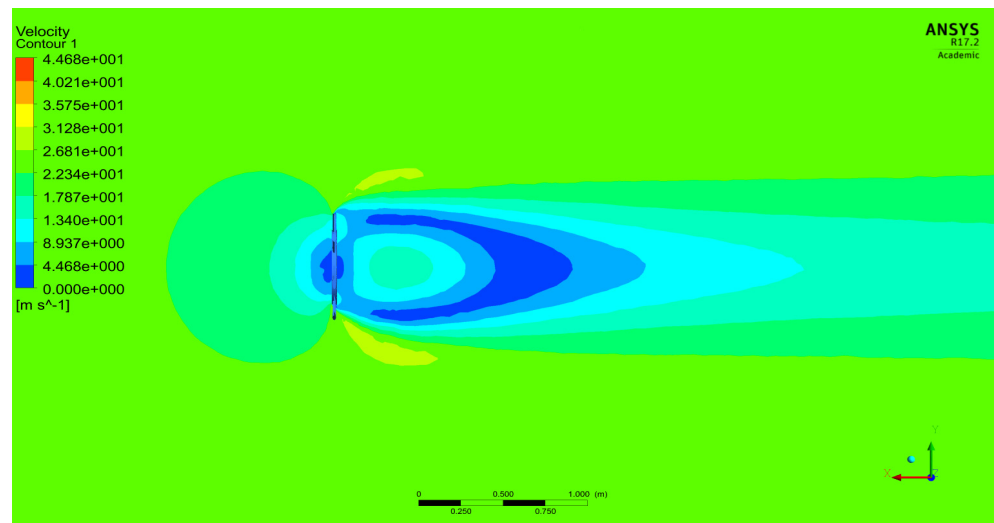
Figure 49. Hydrodynamic velocity variations in and over the Case-2-based Wells turbine.
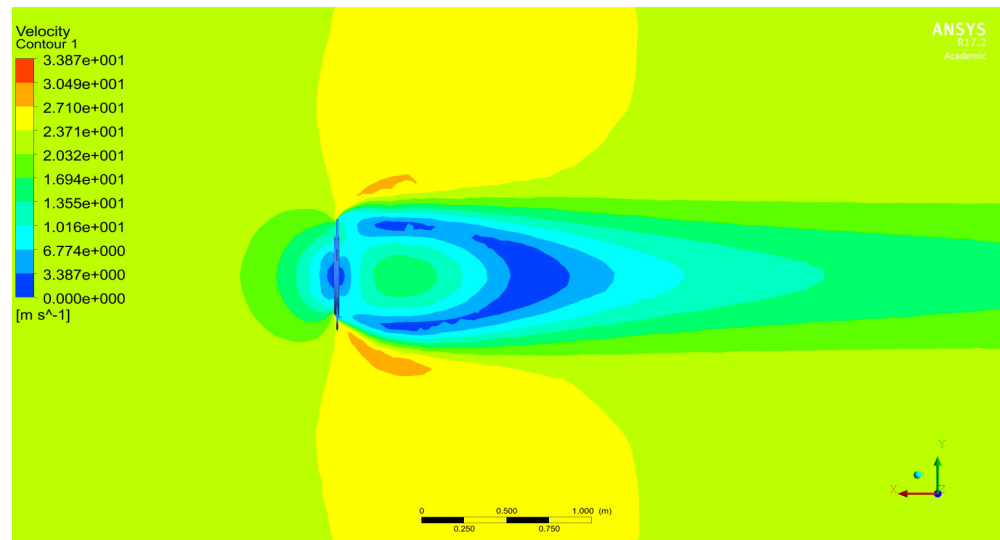
Figure 50. Hydrodynamic velocity variations in and over the Case-1-based Wells turbine.
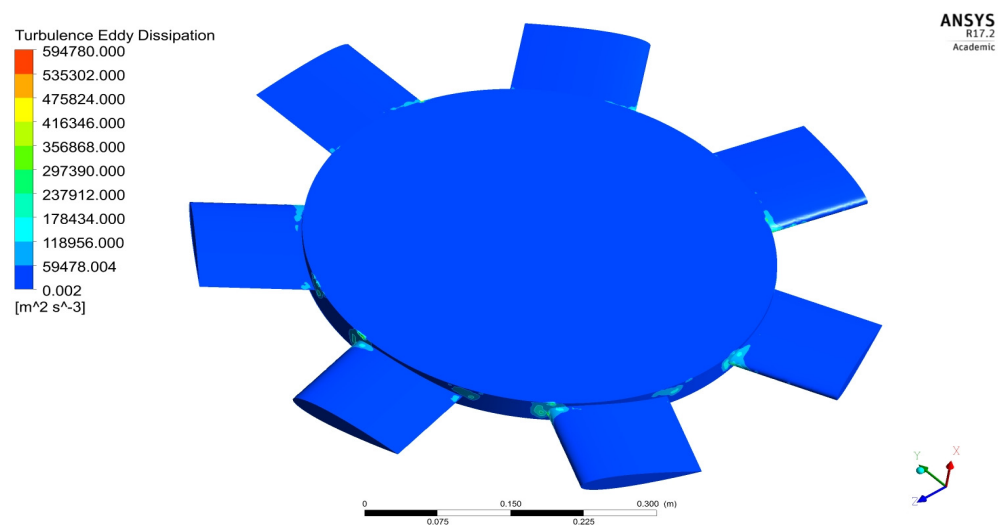

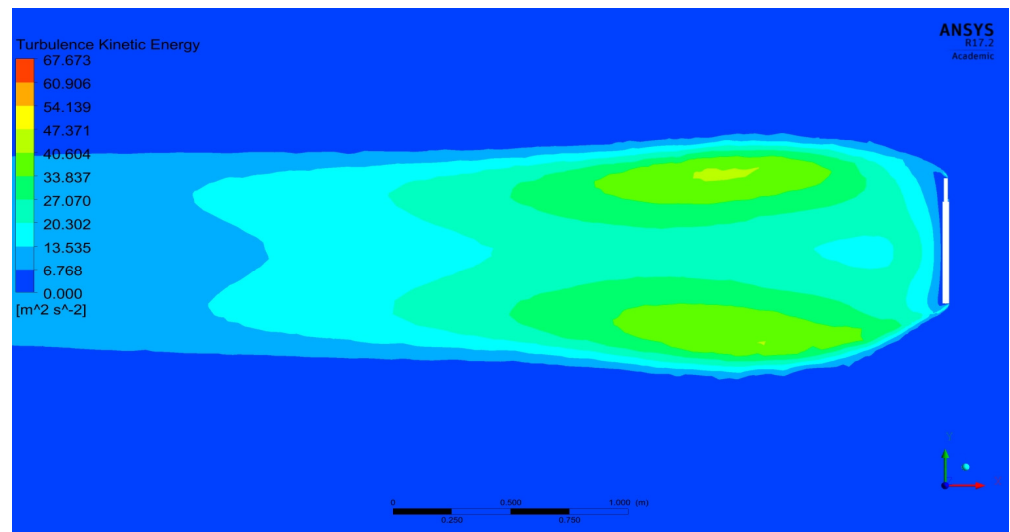**Figure 51.** Turbulence eddy dissipation variations in base case.

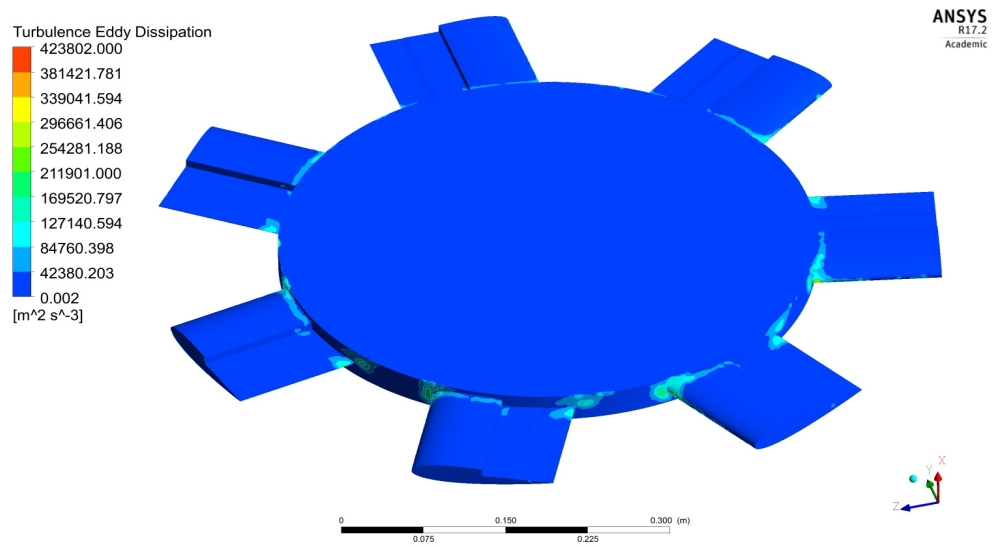**Figure 52.** Turbulence kinetic energy variations in base case.

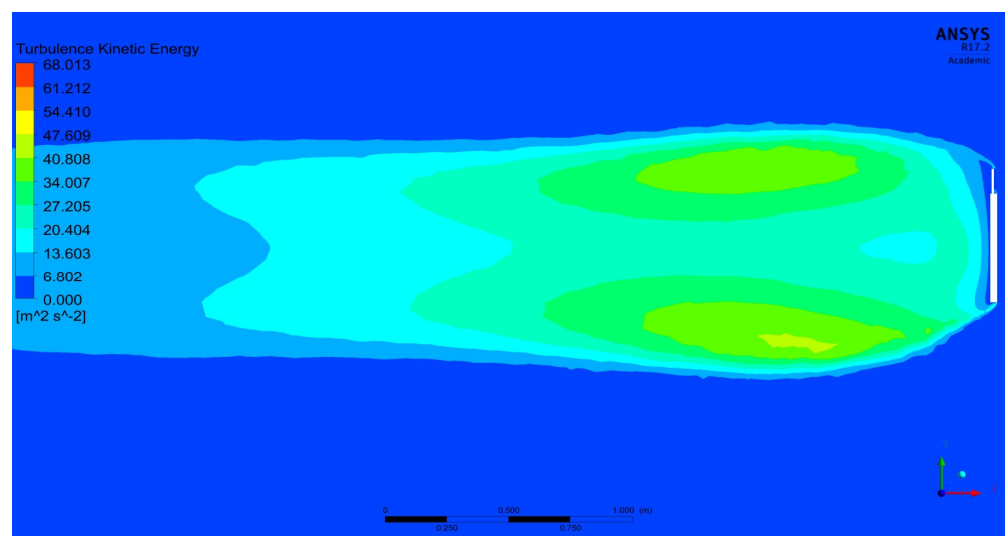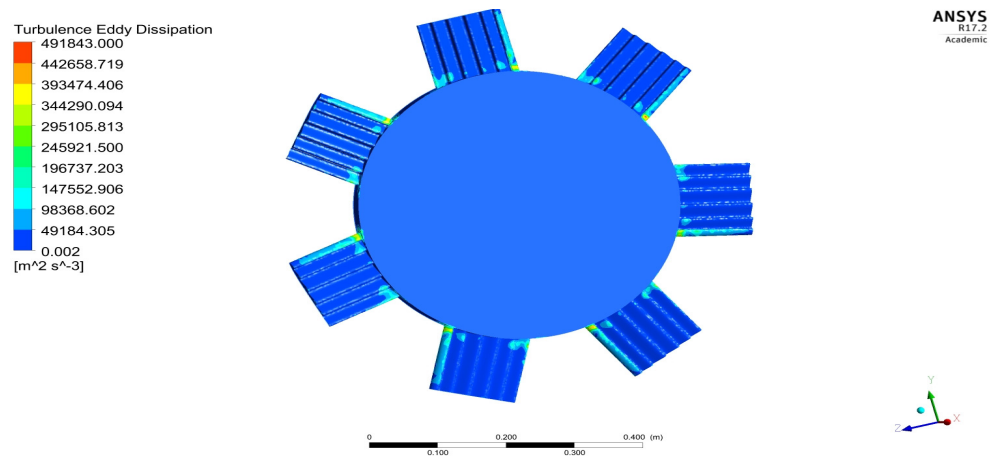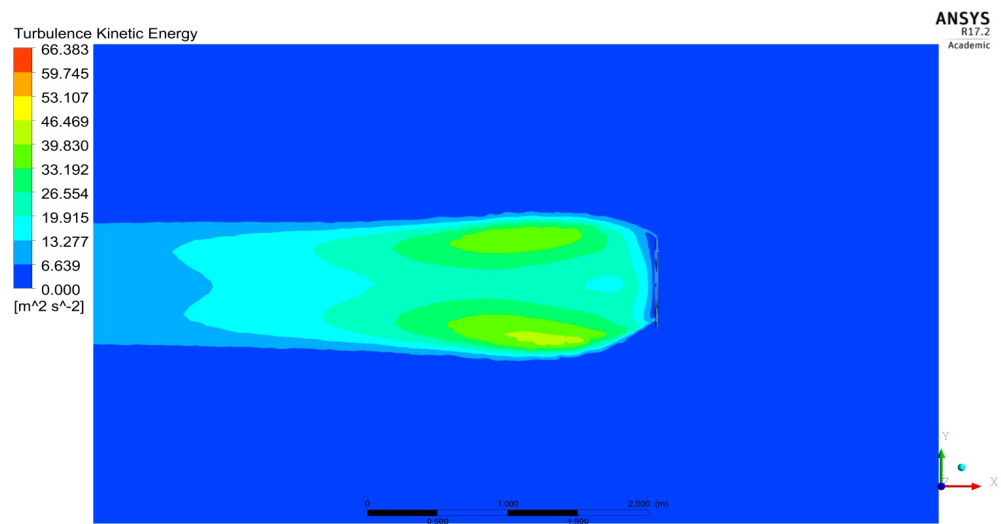**Figure 53.** Turbulence Eddy Dissipation variations in stepped-2 case.

Figure 54. Turbulence kinetic energy variations in stepped-2 case.

**Figure 55.** Turbulence eddy dissipation variations in serration at top-up approach-based case.

Figure 56. Turbulence kinetic energy variations in serration at top-up approach-based case.

3.2. Computational Structural Analyses

Computational structural analyses are performed using the boundary conditions that are mentioned above. In this analysis, total deformation, equivalent elastic strain, equivalent stress, shear stress, normal stress, stress intensity, and strain energy for various materials are obtained to validate the material which can withstand stress, strain, and deformation. The CASE-IV-based Wells turbine model is shortlisted as base computational model for this structural analysis, in which the inlet velocity of hydrodynamic flow simulation is analyzed at 23 m/s. Through the help of one-way coupling-based fluid–structure interaction-based advanced approaches, the aforesaid computational structural analyses are carried out. The typical front view-based structural outcomes such as stress intensity, shear stress, strain energy, normal stress, equivalent stress, equivalent elastic strain, and total deformation are revealed in Figures 57–63.
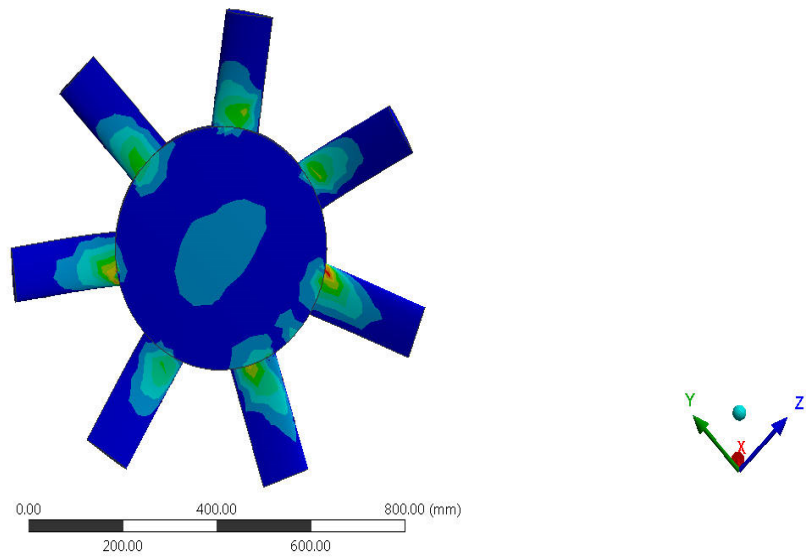
Figure 57. Stress intensity of Wells turbine of the material epoxy carbon woven pre-230.

Figure 58. Shear stress of Wells turbine of the material epoxy carbon woven pre-230.

B: Static Structural
Strain Energy
Type: Strain Energy
Unit: mJ
Time: 1
06-03-2023 13:56

6032.9 Max
5362.6
4692.3
4022
3351.6
2681.3
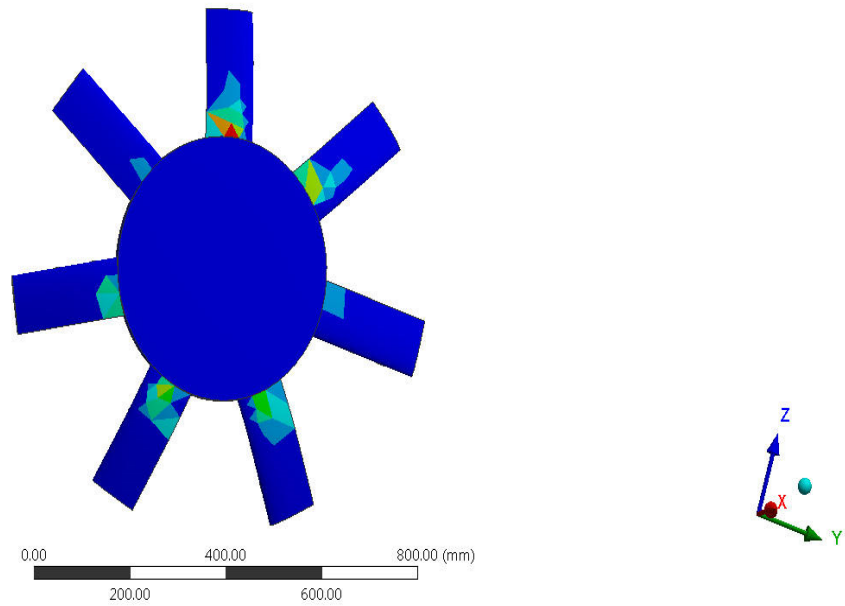2011
1340.7
670.33
7.1669e-6 Min

0.00   400.00   800.00 (mm)
      200.00   600.00

Figure 59. Strain energy of Wells turbine of the material epoxy carbon woven pre-230.

B: Static Structural
Normal Stress
Type: Normal Stress(X Axis)
Unit: MPa
Global Coordinate System
Time: 1
06-03-2023 13:54

373.77 Max
310.6
247.42
184.24
121.06
57.882
-5.2967
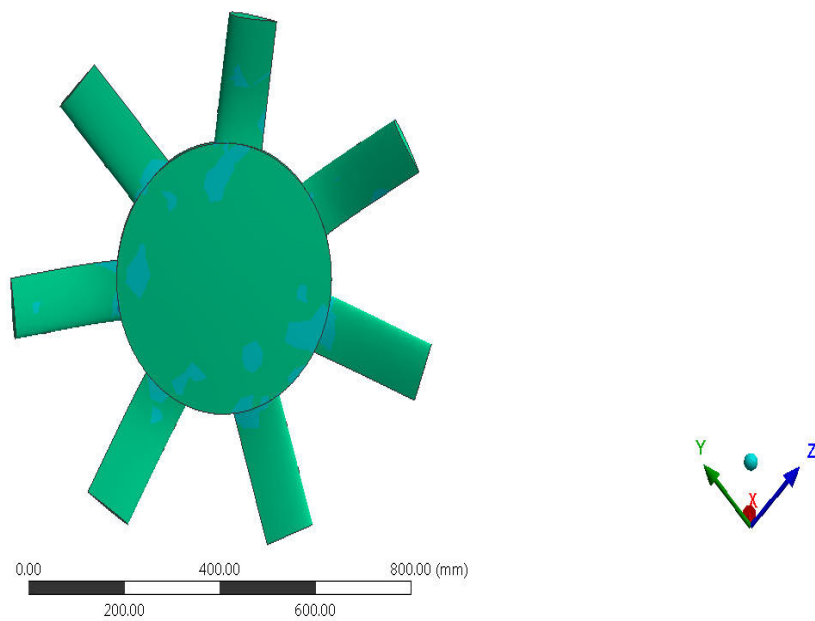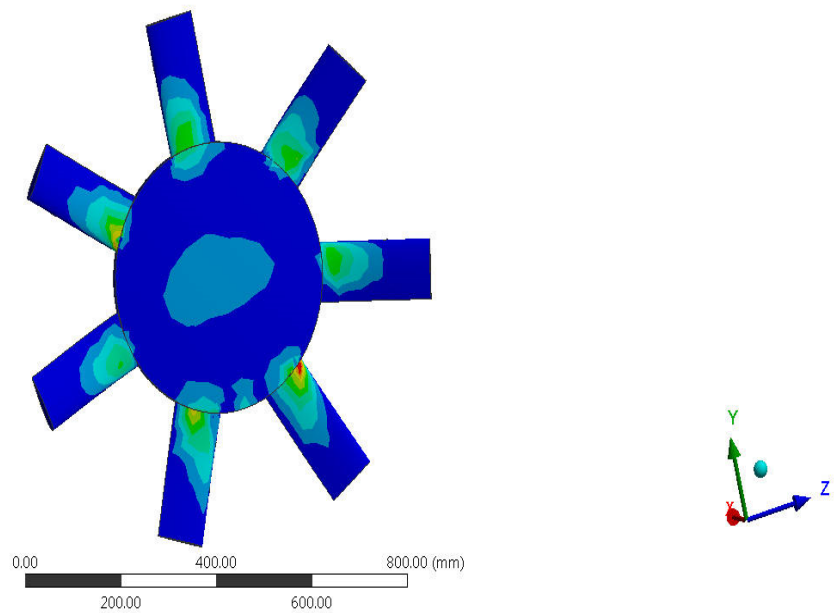-68.475
-131.65
-194.83 Min

0.00   400.00   800.00 (mm)
      200.00   600.00

Figure 60. Normal stress of Wells turbine of the material epoxy carbon woven pre-230.

Figure 61. Equivalent stress of Wells turbine of the material epoxy carbon woven pre-230.
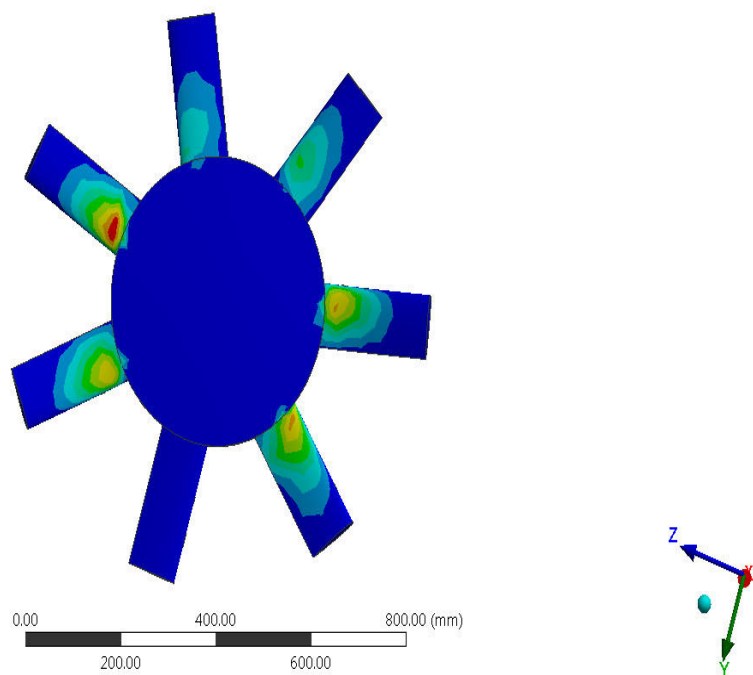
Figure 62. Equivalent elastic strain of Wells turbine of the material epoxy carbon woven pre-230.

Figure 63. Total deformation of Wells turbine of the material epoxy carbon woven pre-230.

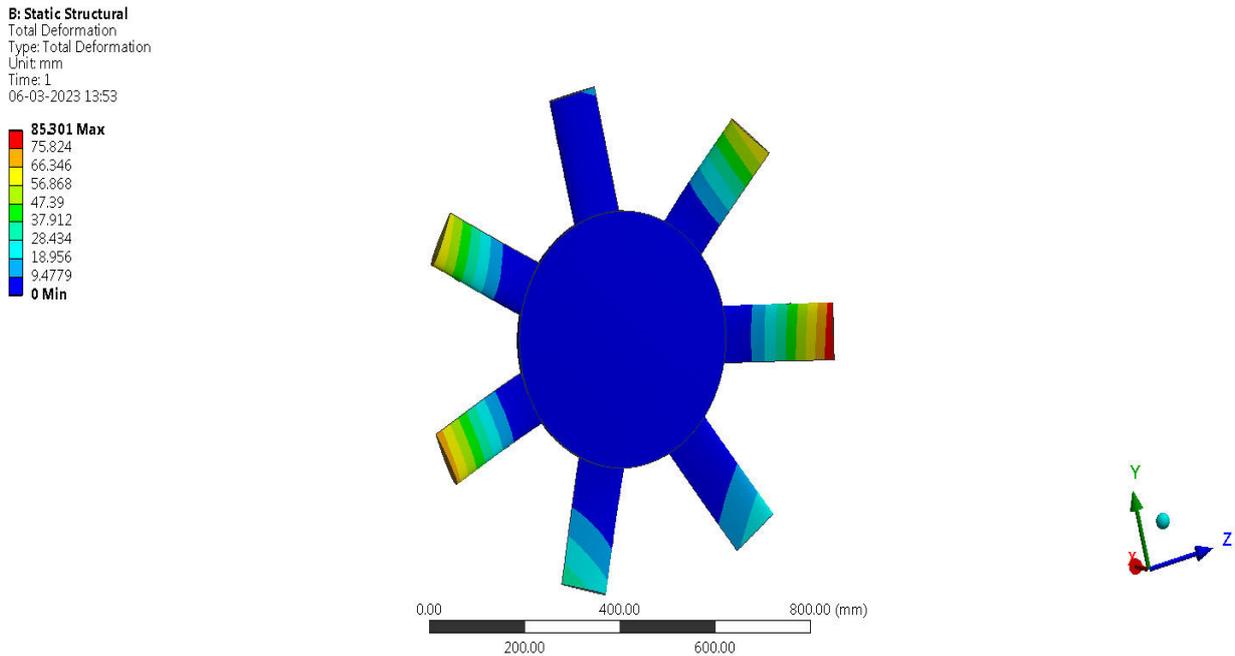The structural outcomes are carefully monitored, wherein the maximum and minimum induced regions are noted. The attained outcomes of maximum and minimum occurred regions are exactly fulfilled with the theoretical concepts of structural physics. In particular, the stress factors are reacted maximally at the fixed end, and so the deformation is maximally reacted at the free end of the Wells turbine. Since the basic structural physics is confirmed, the same computational structural analysis is extended for other lightweight materials such as alloys, CFRP composites, and GFRP composites. The lightweight alloys-based structural outcomes are computed, and so the comprehensive data are listed and shown in Figures 64–70.
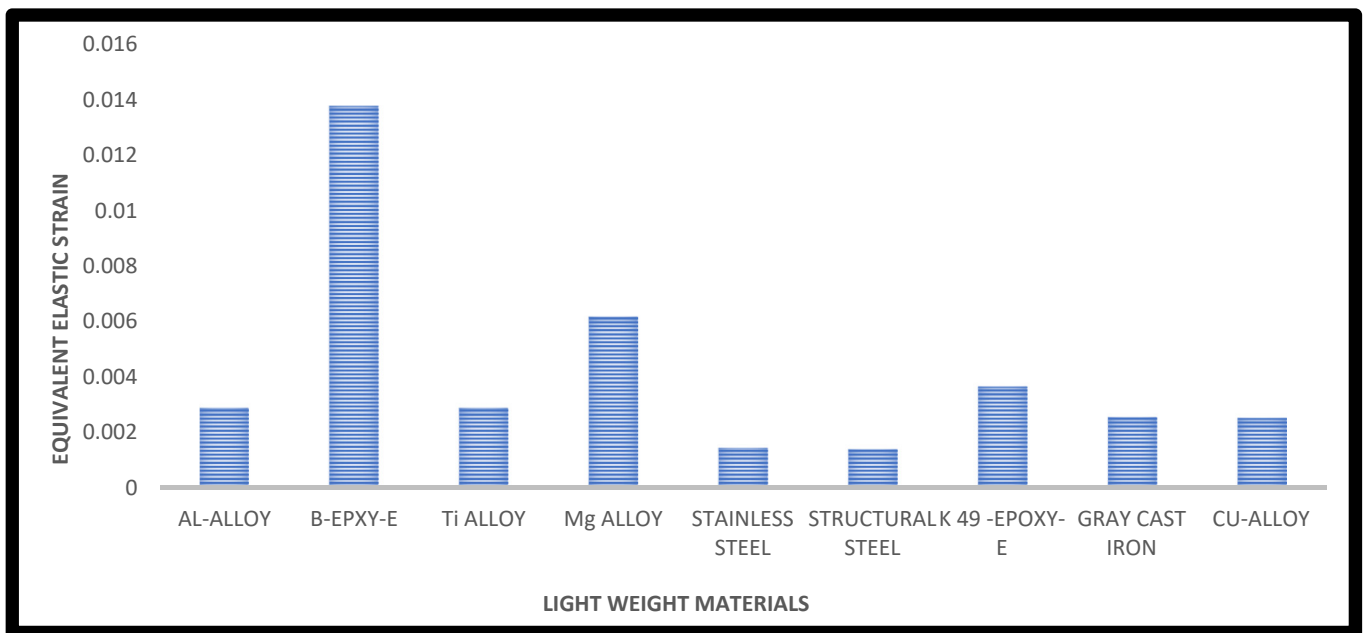
Figure 64. Comprehensive outcomes of equivalent elastic strain for various lightweight alloys and unique composites.
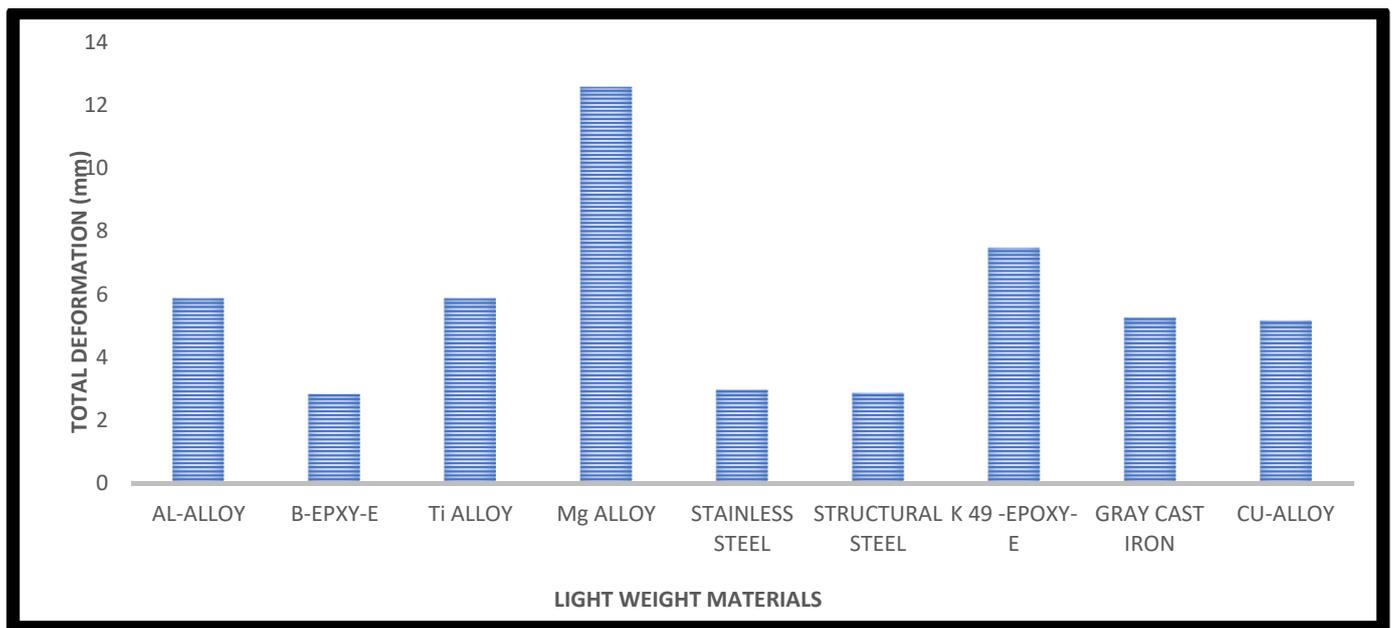
Figure 65. Comprehensive outcomes of total deformation for various lightweight alloys and unique composites.
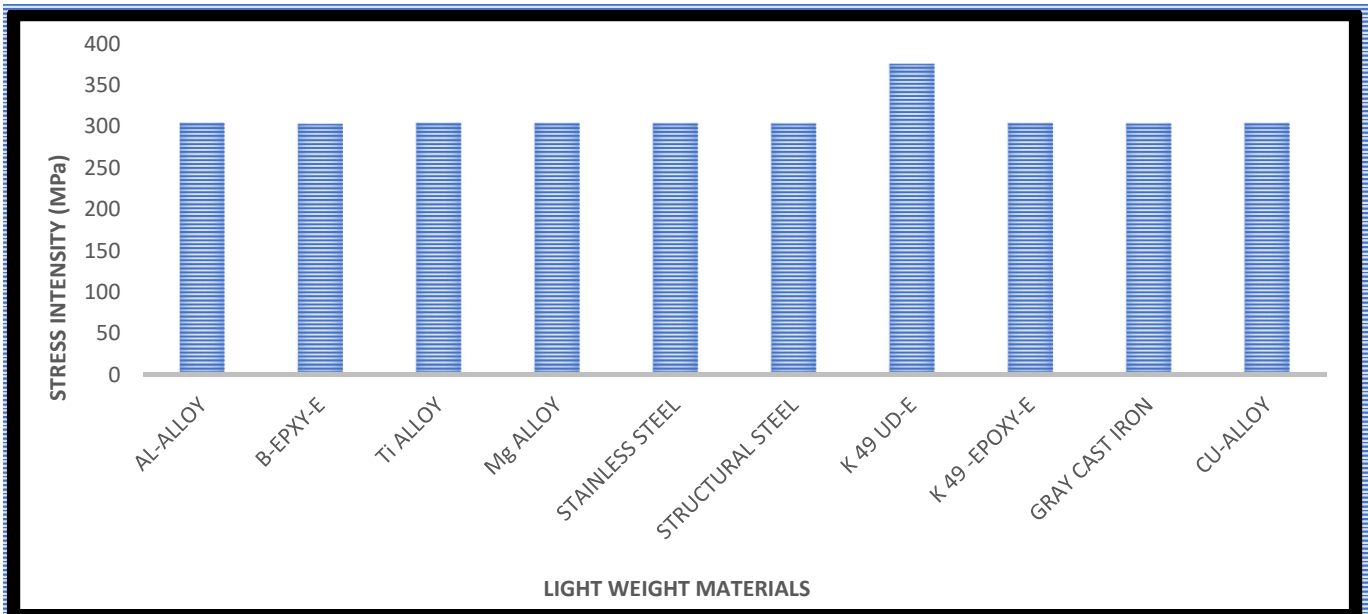
Figure 66. Comprehensive outcomes of stress intensity for various lightweight alloys and unique composites.

Figure 67. Comprehensive outcomes of strain energy for various lightweight alloys and unique composites.
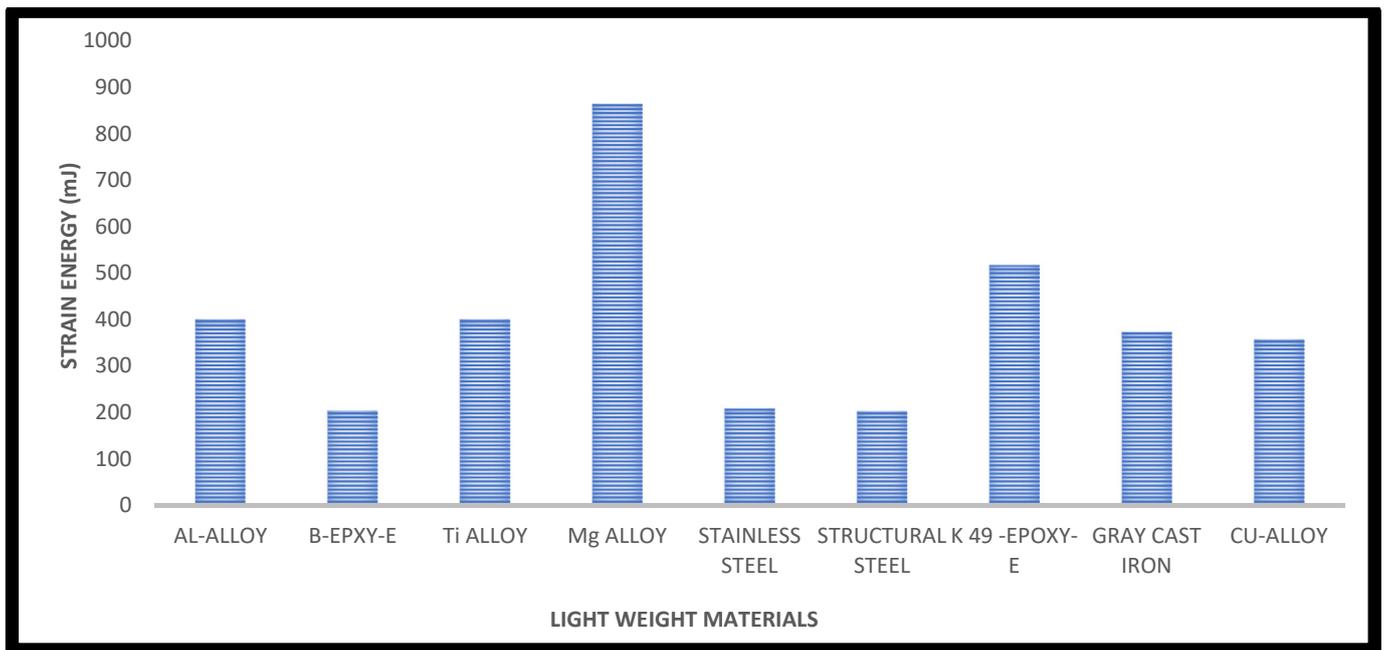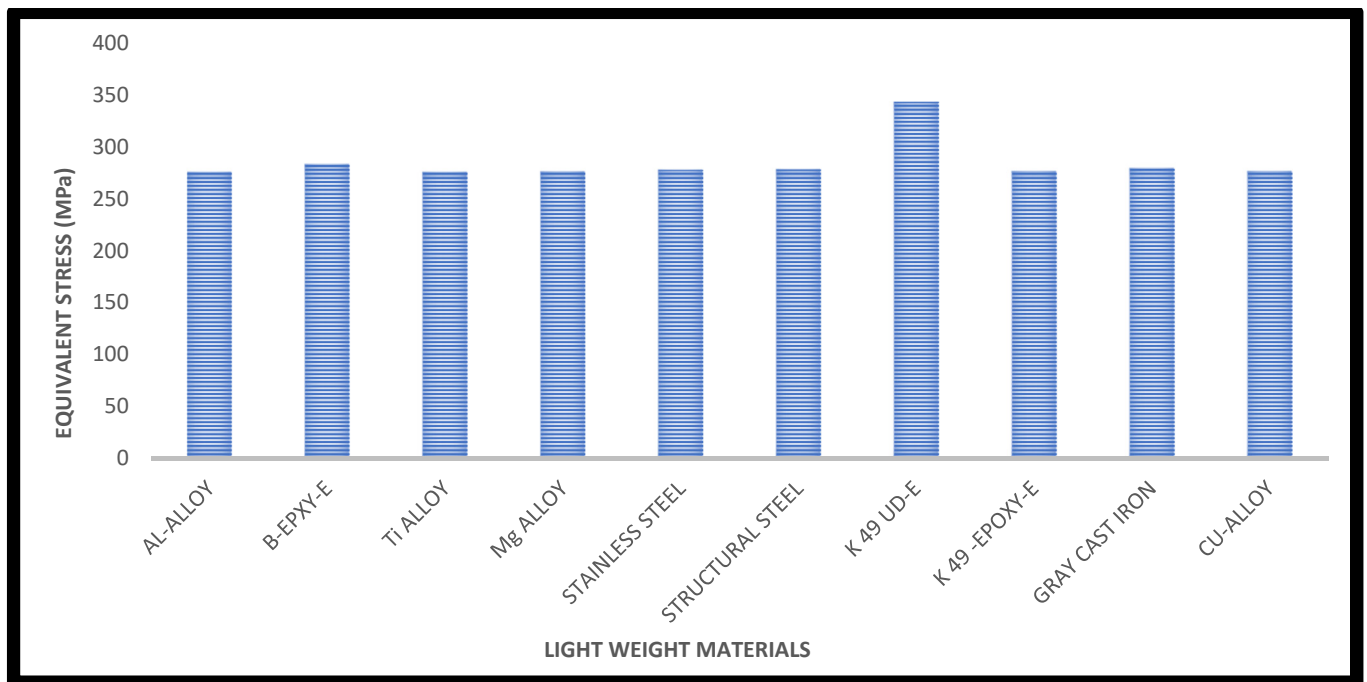

Figure 68. Comprehensive outcomes of equivalent stress for various lightweight alloys and unique composites.
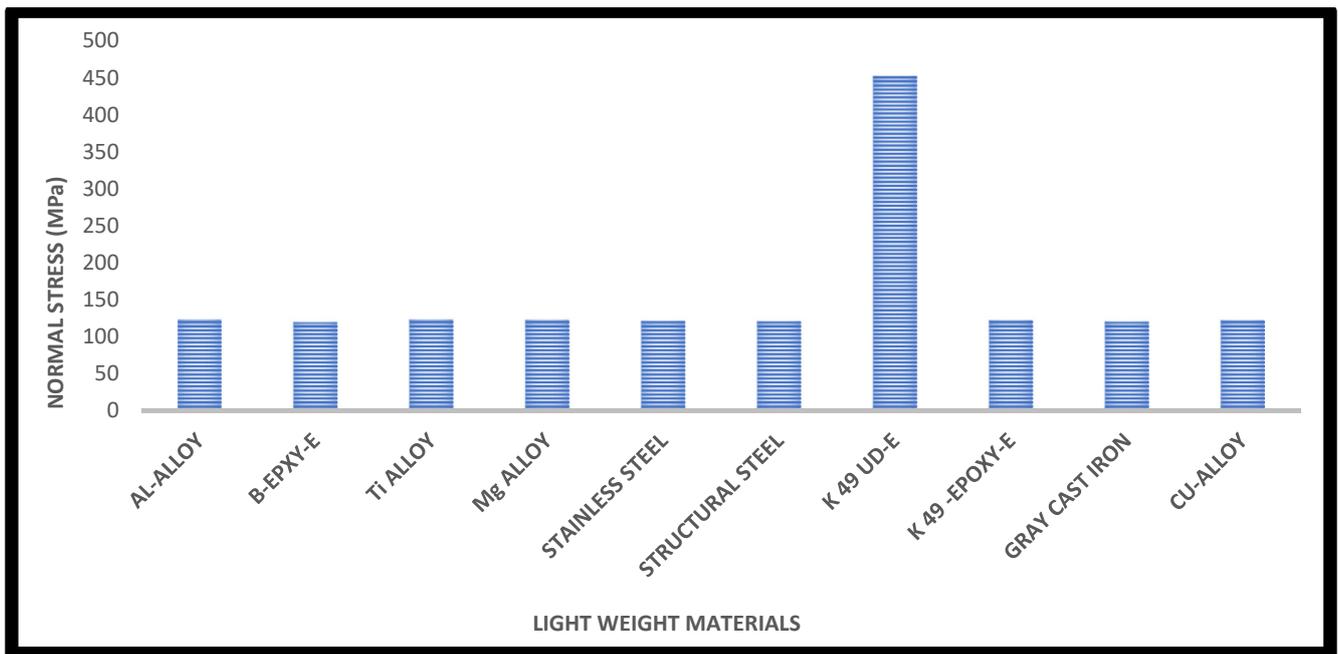
Figure 69. Comprehensive outcomes of normal stress for various lightweight alloys and unique composites.
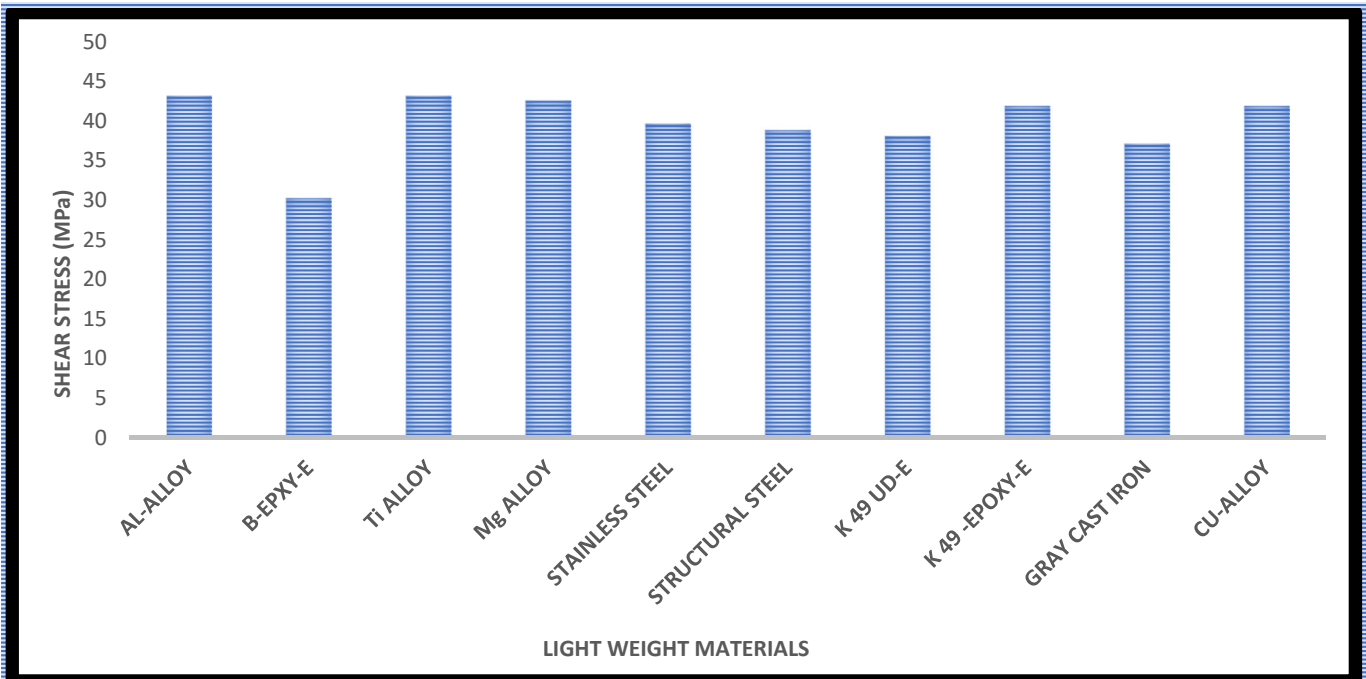
Figure 70. Comprehensive outcomes of shear stress for various lightweight alloys and unique composites.

Figure 64 shows the equivalent elastic strain results of all lightweight materials except Kevlar-49-Epoxy because it has more equivalent elastic strain when compared to other materials, which is shown in the above bar chart. The equivalent elastic strain obtained from Kevlar-49-Epoxy is 0.055941 at the inlet velocity of 23 m/s.

Figure 65 depicts the total deformation results of all lightweight materials except Kevlar-49-Epoxy because it is highly deformed when compared to other materials, which is shown in the above bar chart. The total deformation obtained from Kevlar-49-Epoxy is 105.82 mm at the inlet velocity of 23 m/s.

The stress intensity outcomes of all the lightweight alloys and few unique composites are systematically revealed in Figure 66. With the consideration of low-stress-induced level, the boron fiber and epoxy resin-associated composite performs well.

Figure 67 shows the strain energy results of all lightweight materials except Kevlar-49-Epoxy because it has more strain energy when compared to other materials, which is shown in the above graph. The strain energy obtained from Kevlar-49-Epoxy is 7402.7 mJ at the inlet velocity of 23 m/s.

The equivalent stress-, normal stress-, and shear stress-based structural outcomes are computed for the shortlisted lightweight alloys and few unique composites. The respective comprehensive outcomes are revealed in Figures 68–70. Additionally, the deformed magnitudes of the imposed lightweight materials based wells turbine are systematically revealed in Figure 71. Since the load and supports are common for all the materials, the low-reacting material is superior to provide a high lifetime. Henceforth, the boron fiber and epoxy resin-associated composite reacts in a less effective manner, and so the same lightweight material is chosen as the best material.
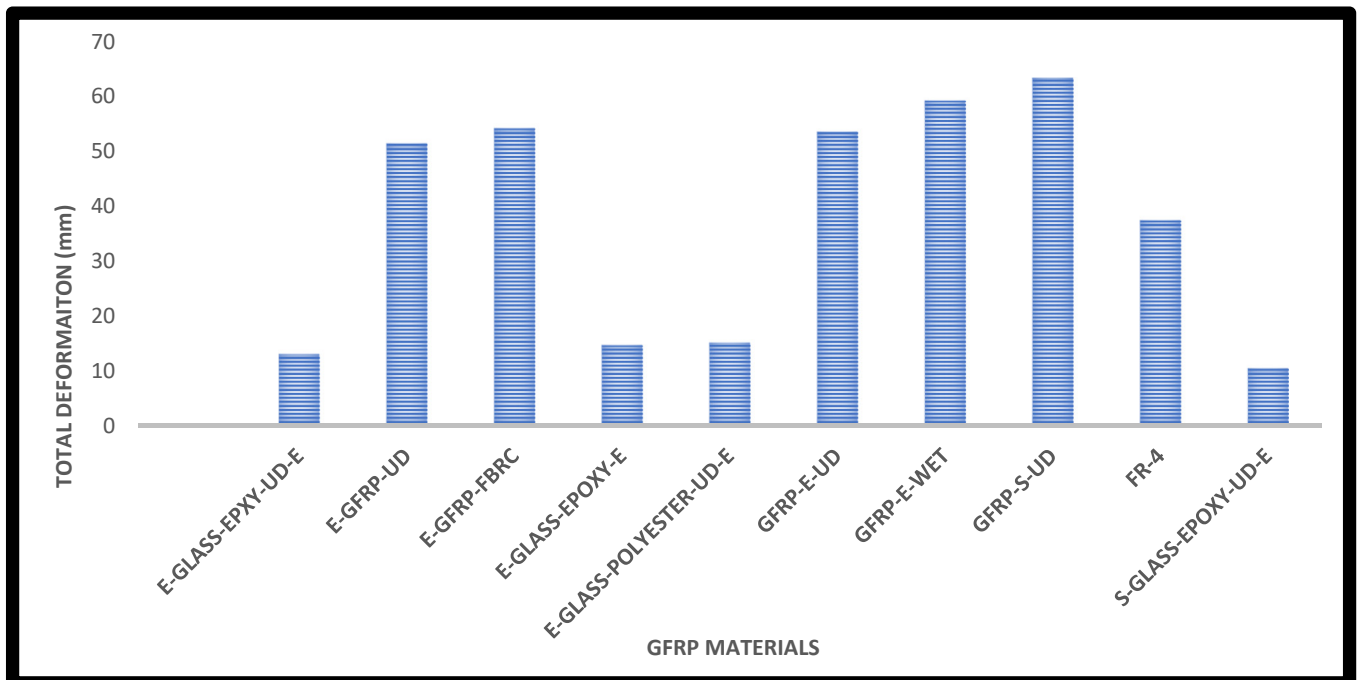
Figure 71. Comprehensive outcomes of total deformation for various GFRP composites.

After the successful completion of first case of comprehensive structural studies, the second comprehensive structural investigations are computed for various lightweight GFRP composites. The imposed GFRP composites are E-GFRP-UD-, E-GFRP-Fabric-, E-GFRP-UD-Polyester-, E-GFRP-Wet-, S-GFRP-UD-, and FR-4-GFRP-based composites and their associates' productions. The comprehensive structural outcomes of the third case that contains GFRP-based outcomes are revealed in Figures 72–77.

Figure 72. Comprehensive outcomes of equivalent elastic strain for various GFRP composites.

Figure 73. Comprehensive outcomes of equivalent stress for various GFRP composites.

Figure 74. Comprehensive outcomes of stress intensity for various GFRP composites.

Figure 75. Comprehensive outcomes of strain energy for various GFRP composites.

Figure 76. Comprehensive outcomes of normal stress for various GFRP composites.
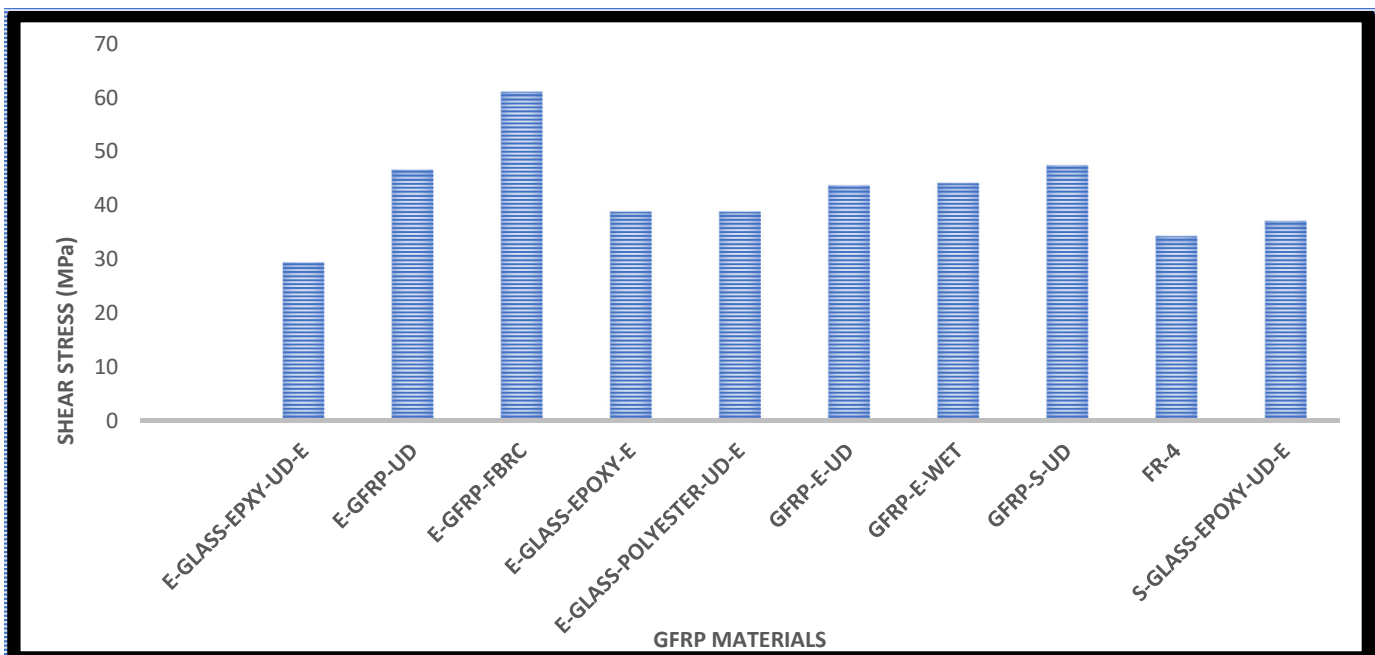
Figure 77. Comprehensive outcomes of shear stress for various GFRP composites.

From Figures 72–77, it is observed that the S-GFRP-UD-Epoxy-based composite reacts in a less effective manner than the other GFRP composites. Henceforth, the same S-GFRP-UD-Epoxy-based composite is chosen as the best performer. After the successful completion of the second case of comprehensive structural studies on GFRP composites, the third comprehensive structural investigations are computed for various lightweight CFRP composites. The comprehensive structural outcomes of the third case that contains CFRP-based outcomes are revealed in Figures 78–84.
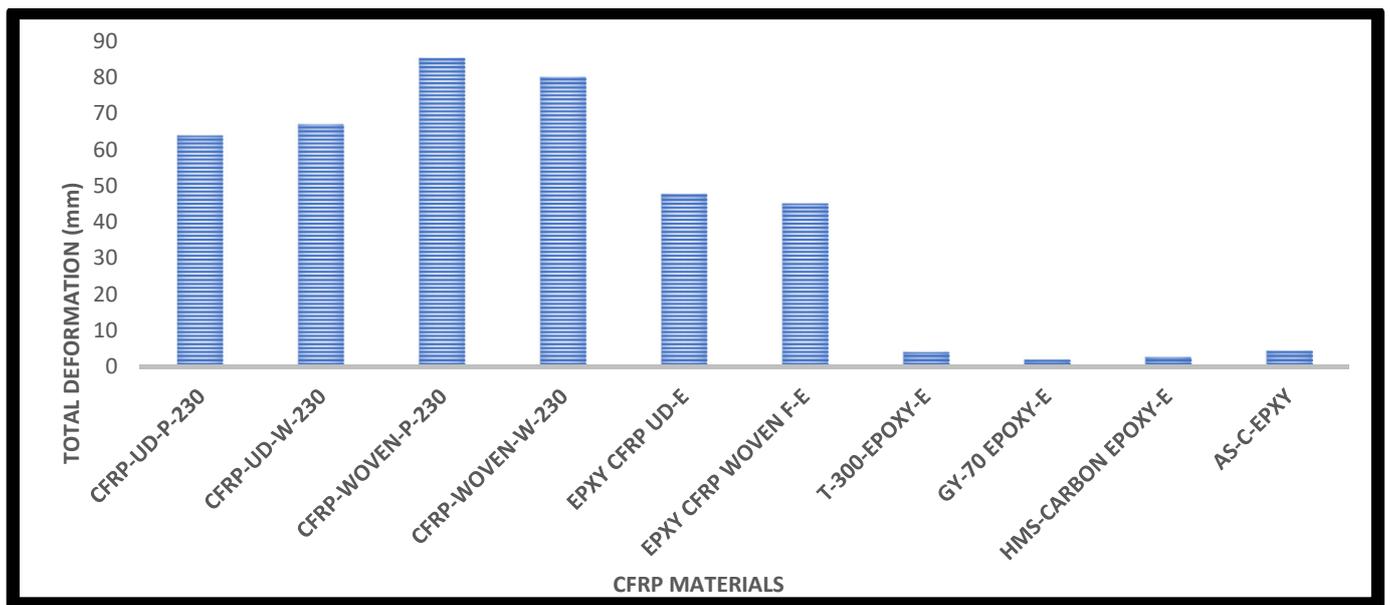
Figure 78. Comprehensive outcomes of total deformation for various CFRP composites.
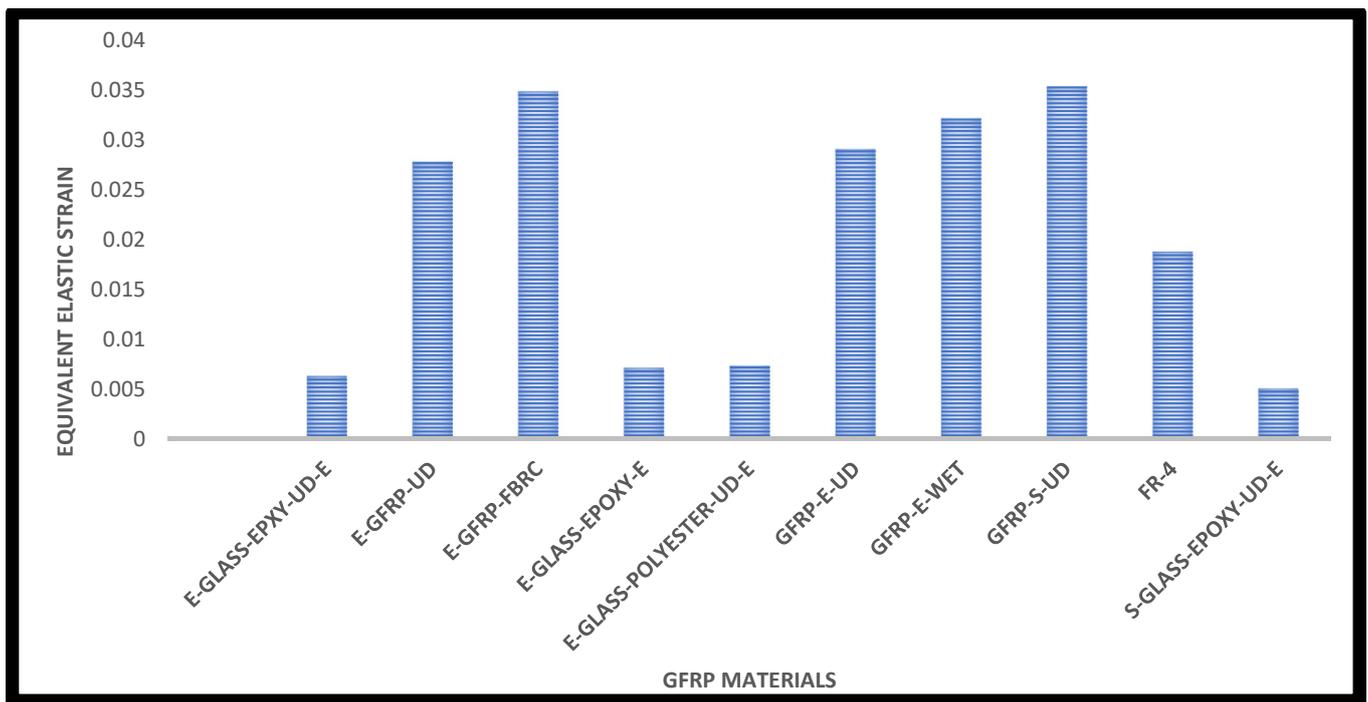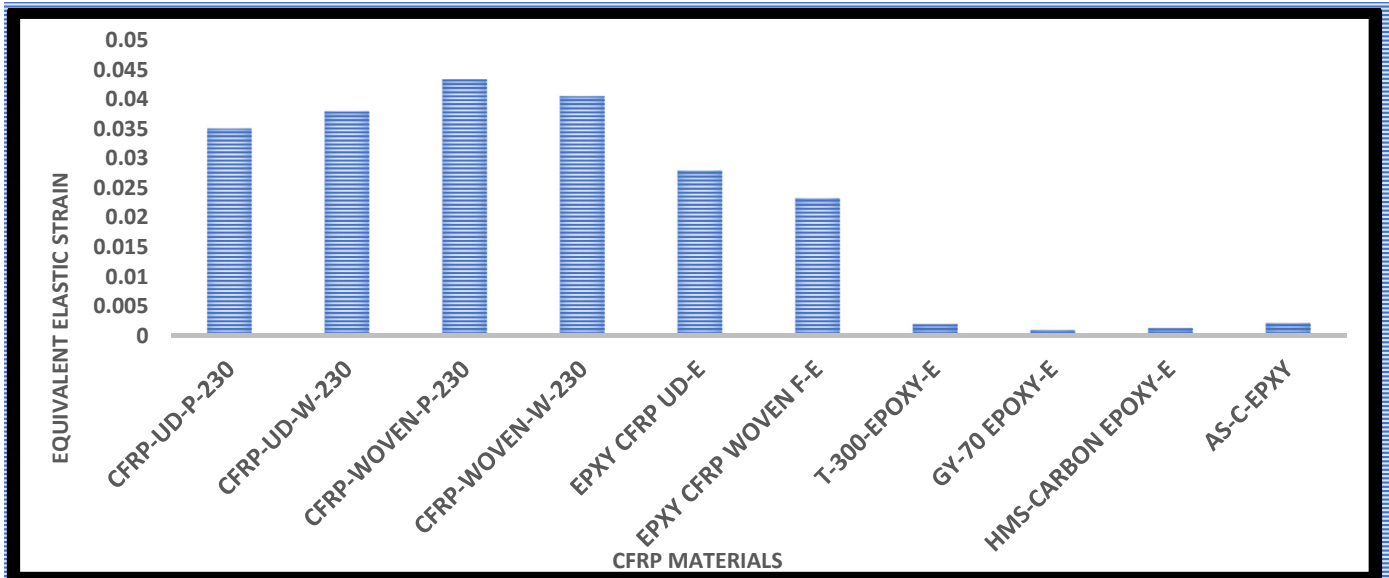

Figure 79. Comprehensive outcomes of equivalent elastic strain for various CFRP composites.
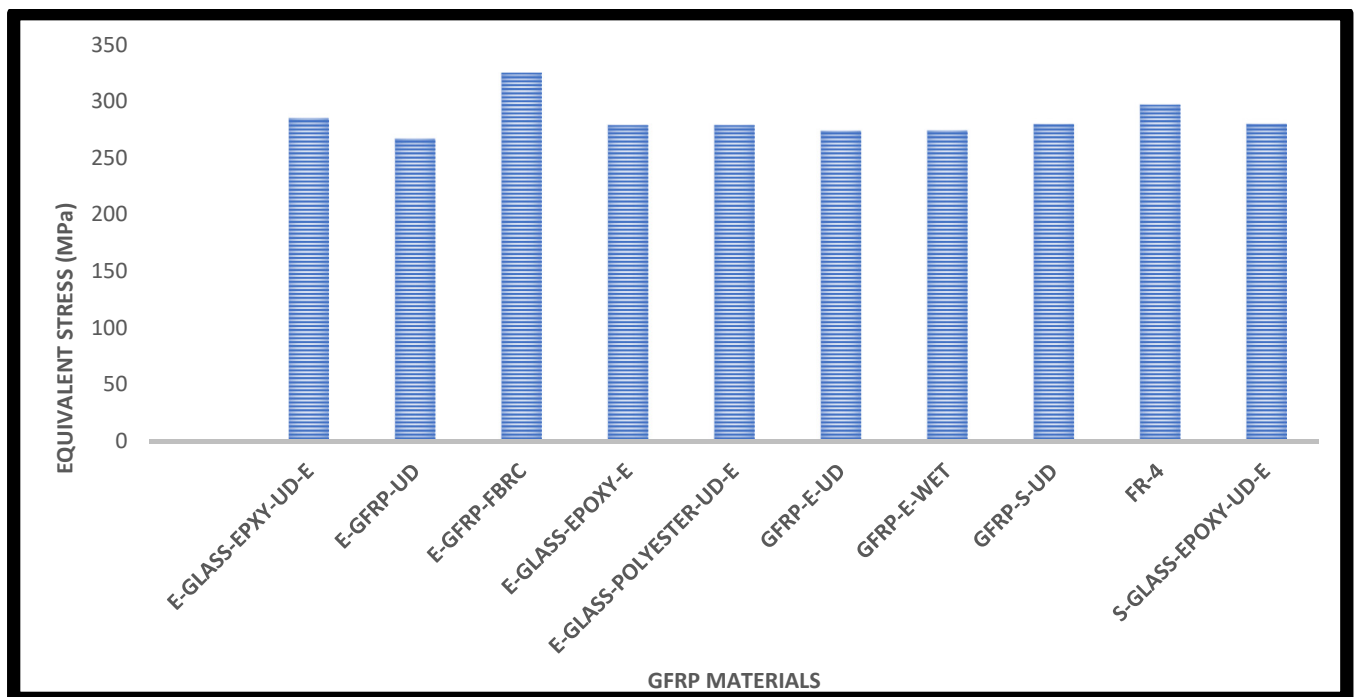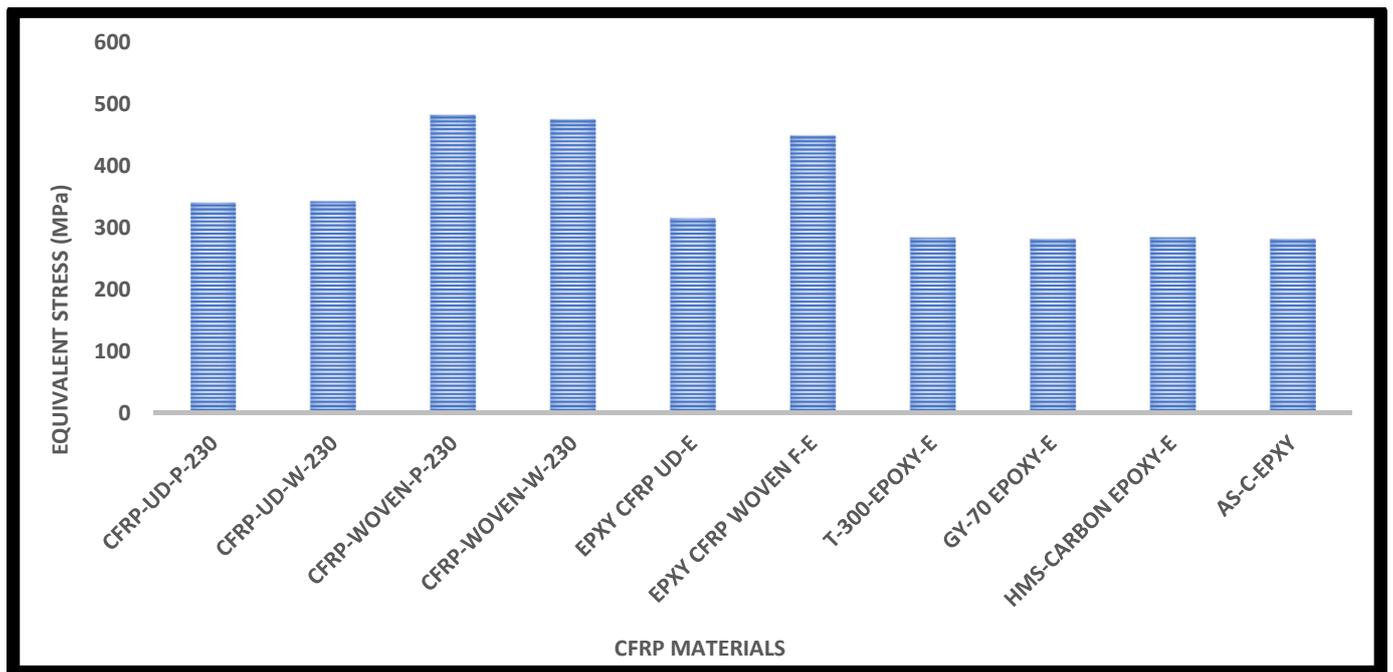
Figure 80. Comprehensive outcomes of equivalent stress for various CFRP composites.
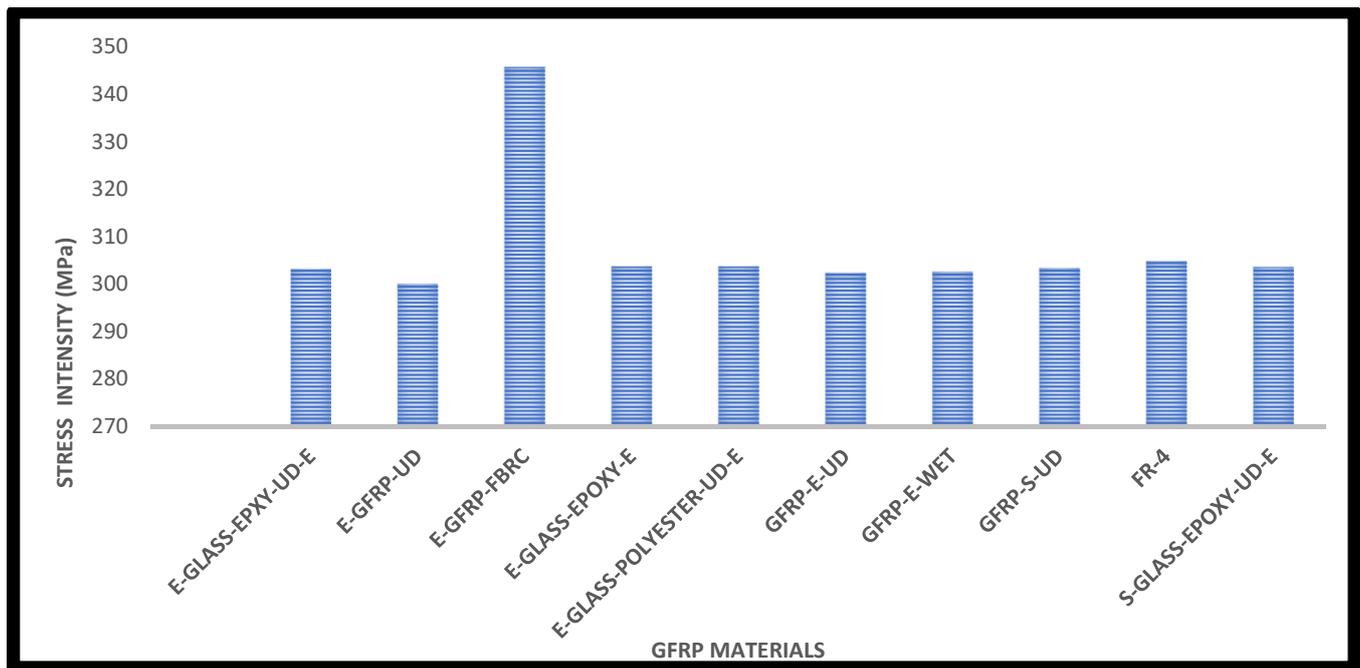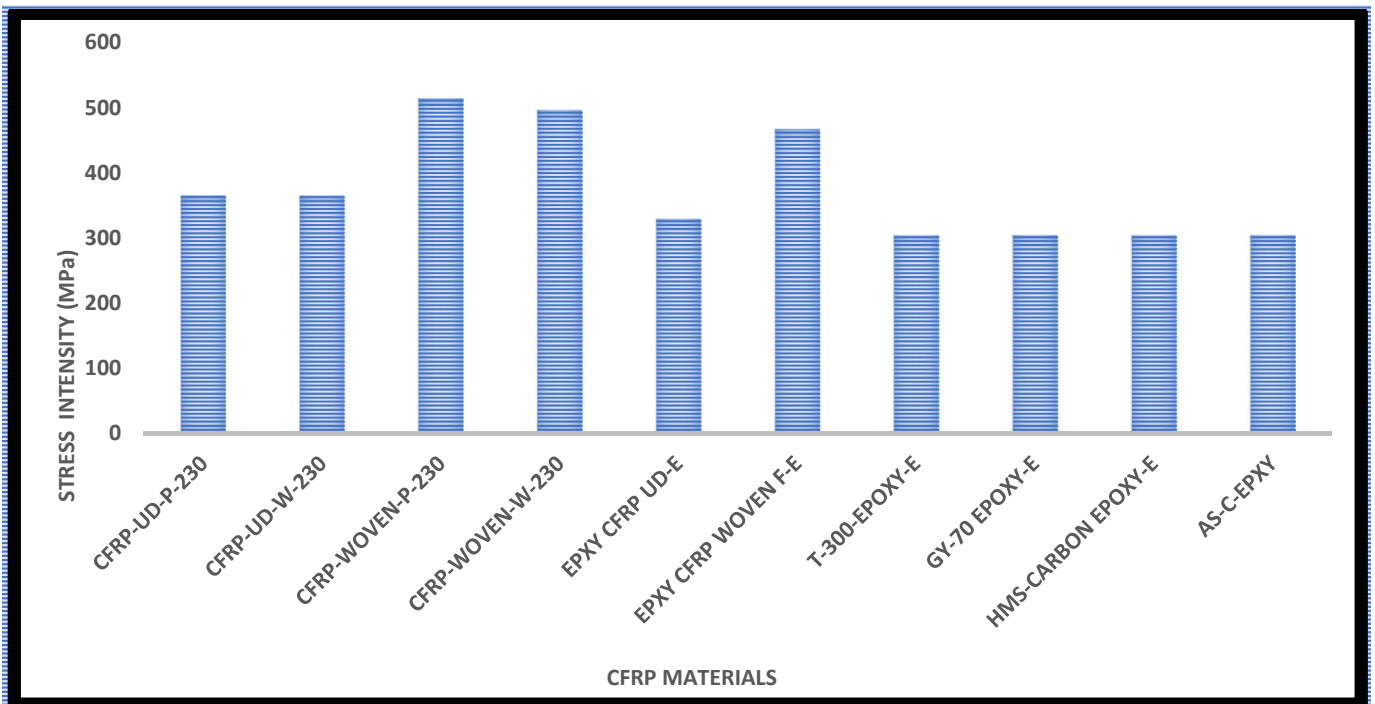

Figure 81. Comprehensive outcomes of stress intensity for various CFRP composites.
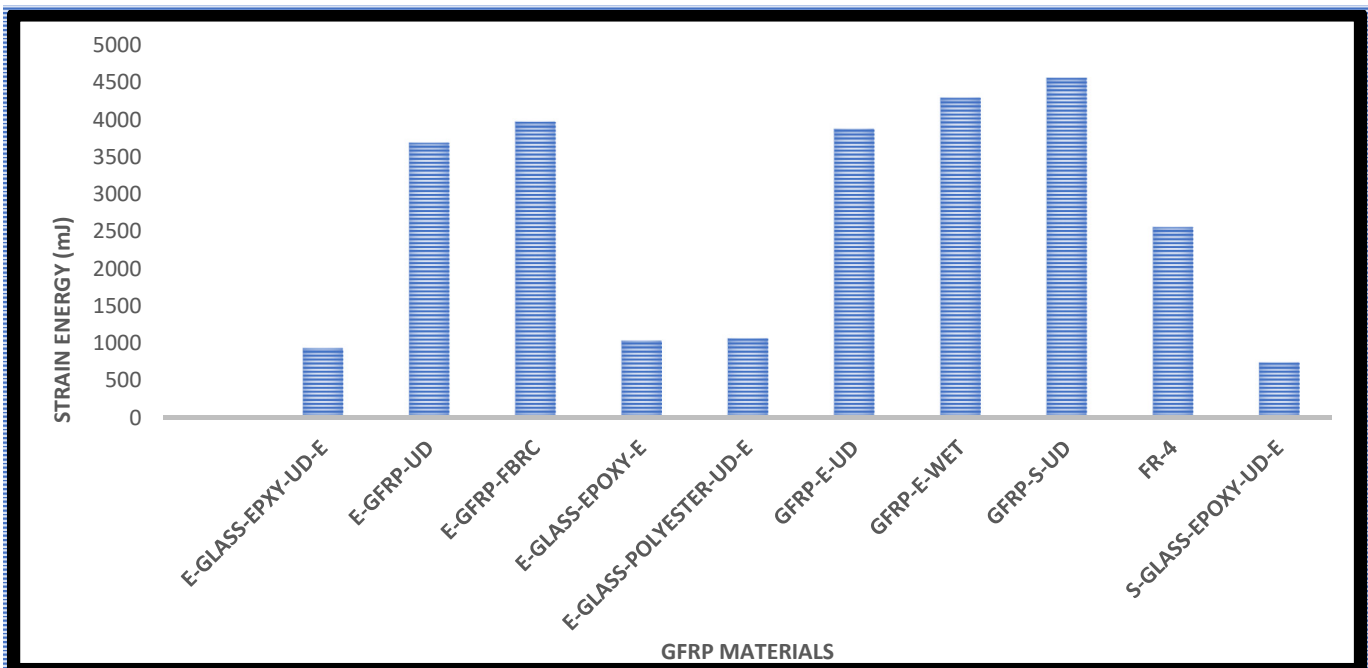
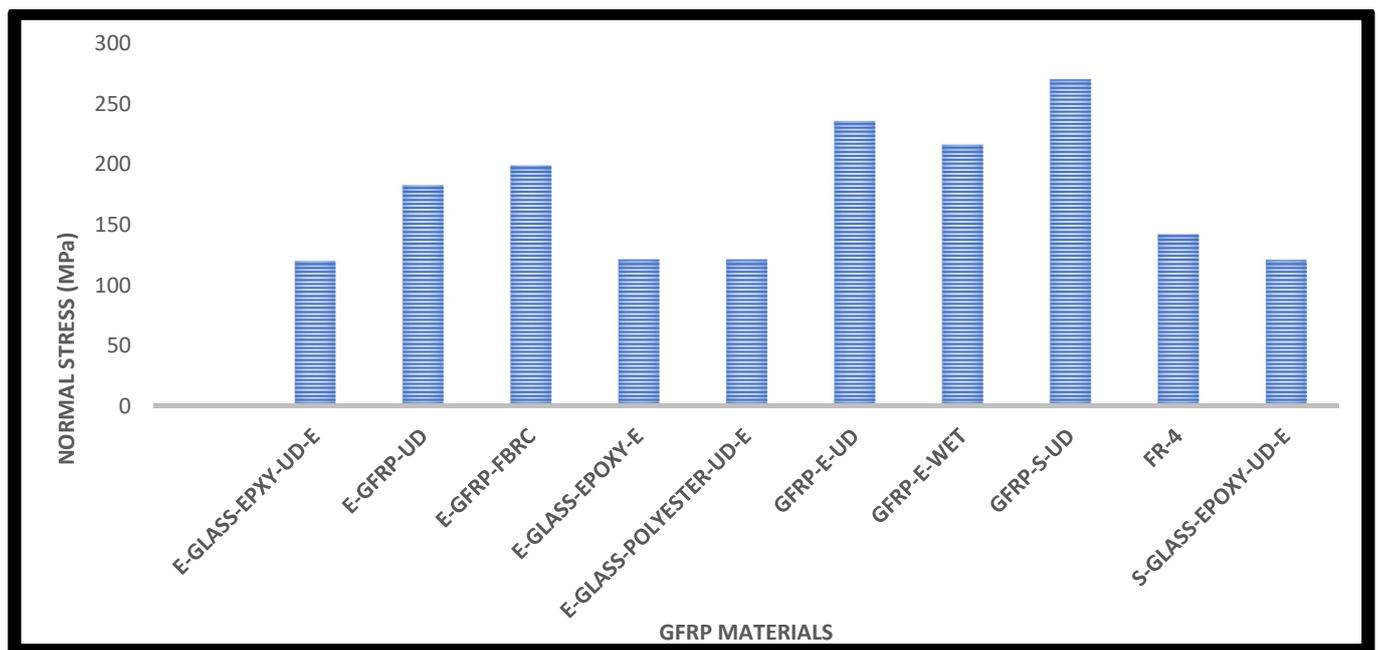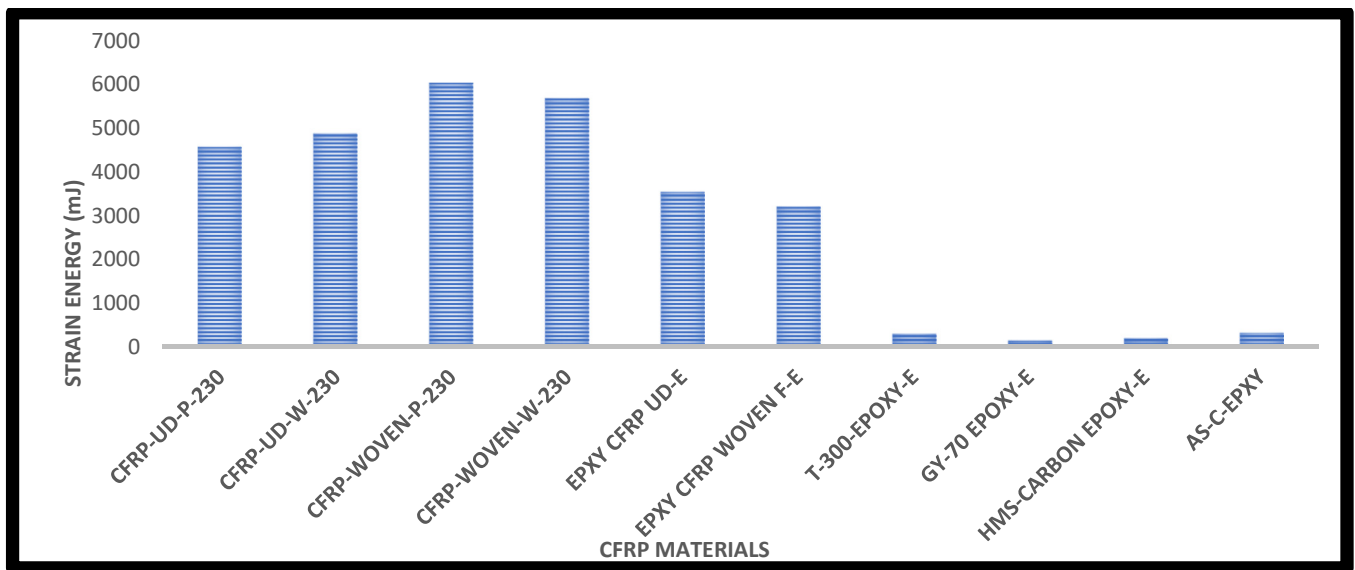**Figure 82.** Comprehensive outcomes of strain energy for various CFRP composites.
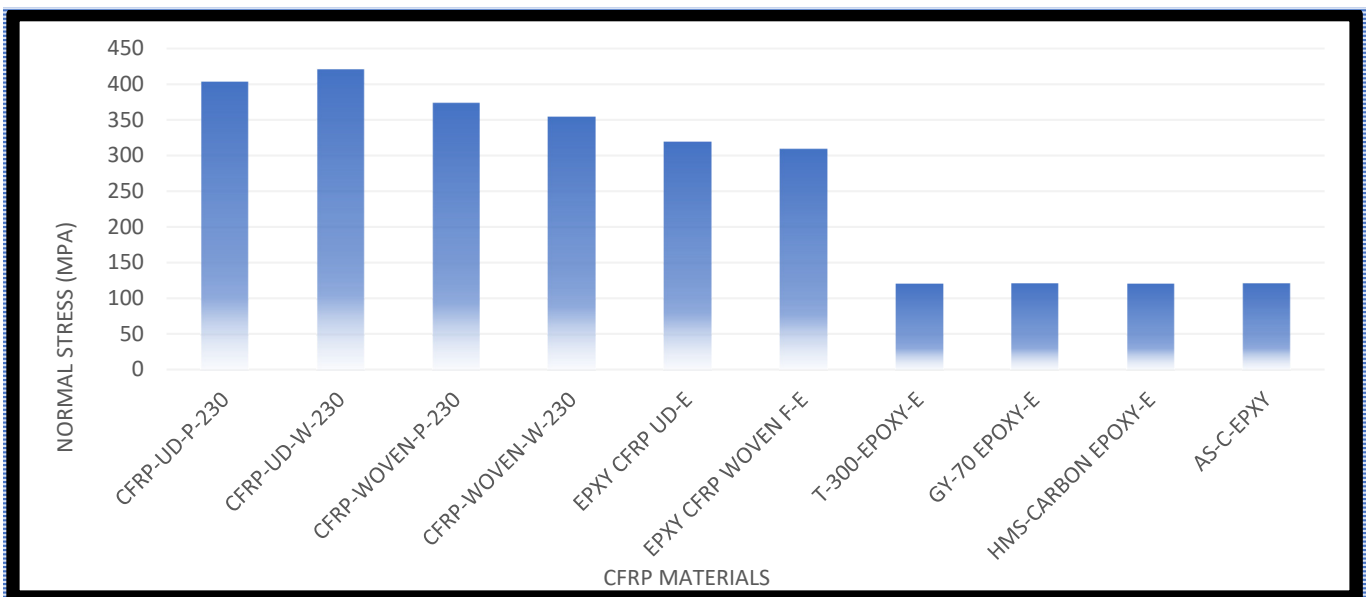
Figure 83. Comprehensive outcomes of normal stress for various CFRP composites.

Figures 78–84 depict the graphical representation of structural analyses of the Wells turbine at the inlet velocity of 23 m/s (deep water velocity), which comprises total deformation, equivalent elastic strain, equivalent stress, stress intensity, strain energy, normal stress, and shear stress with the respective CFRP materials. By comparing the above-shown CFRP materials, T-300 epoxy- and GY-70 epoxy-based composites in particular performed better than other materials. Since the load-resisting behavior of these shortlisted lightweight materials is high, the reaction is generated in a less effective manner than other materials.
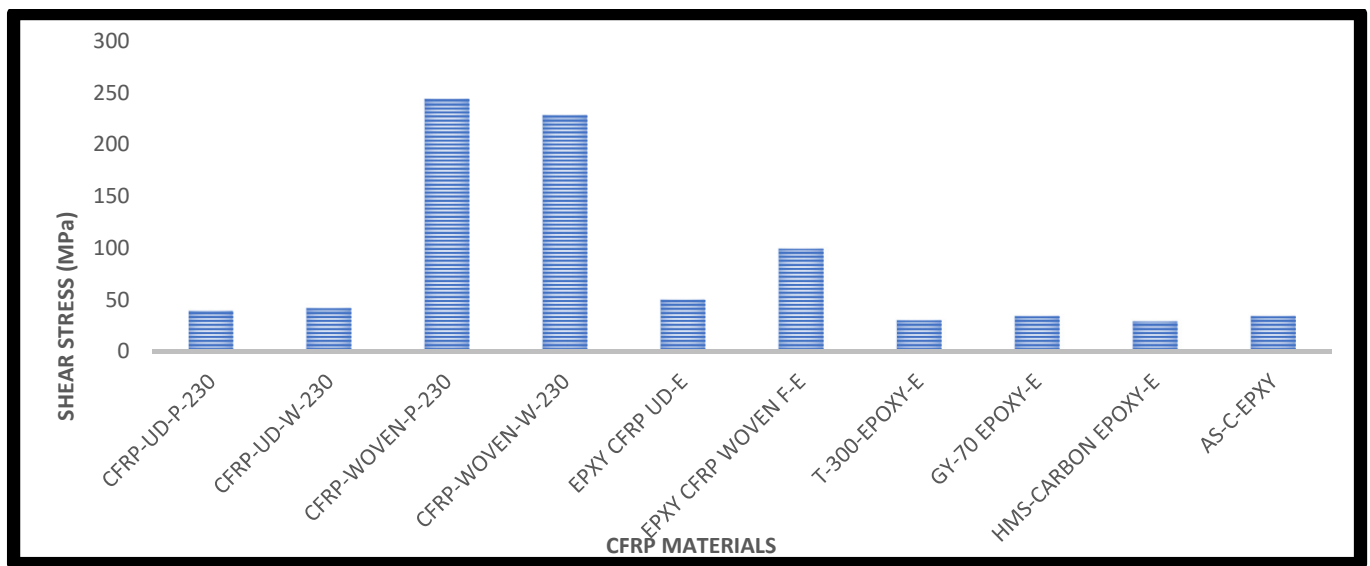
Figure 84. Comprehensive outcomes of shear stress for various CFRP composites.

3.3. Estimation of Power from Energy Harvester

Important steps in this evaluation include picking and calculating PVEH patches. Several common and hybrid materials were analyzed in ANSYS. In the first step, the authors calculated the power of various materials. Then, the computations were carried out in two stages: an intermediate power estimate and a final power estimate. Equation (12) necessitates the first iteration of intermediate power extraction.

$$P_{\text{Intermediate}}^{\text{Hybrid Wells Turbine}} = d_{\text{lwm}}^2 w^2 f^2 \frac{18 * T_{PL}}{\left[(W_{L-WT}) * (L_{PL})^2 * ([t_{WT}] + [T_{PL}])^4 \right]} \frac{\rho_{\text{lwm}}}{[1 + f * \varepsilon * (\rho_{\text{lwm}})]} \tag{12}$$

$$P_{\text{Final}}^{\text{Hybrid Wells Turbine}} = \left(P_{\text{Intermediate}}^{\text{Hybrid Wells Turbine}} \right) \left(\frac{(0.44 * L)^5}{36} - \frac{L(0.44 * L)^4}{6} + \frac{5L^2(0.44 * L)^3}{12} - \frac{L^3(0.44 * L)^2}{2} \frac{L^4(0.44 * L)}{4} \right) \tag{13}$$

For the purpose of determining the power output of the PVEH patches, the previously described mathematical procedures (Equations (12) and (13)) must be utilized. Table 10 provides a summary of the findings that were acquired through the utilization of a variety of lightweight materials to harvest energy from the rotor span.

Table 10. Estimated energy outcome on 100% of the blade span.

Materials	Energy Extracted (W)	Materials	Energy Extracted (W)
KFRP-49-UD	3375.524253	GFRP-E-Wn	1705.544864
CFRP-Wn-wet	3849.998201	GFRP-E-UD	2813.393605
CFRP-wet-UD	5148.895683	GFRP-E-wet	2250.131784
CFRP-UD-Pg	5294.984336	GFRP-S-UD	2960.020325
CFRP-Wn-Pg	3978.721358	GFRP-FR-4-Wn	1545.139361

Table 11 shows the total output power of CASE-IV for the inlet velocity of 12.10 m/s using different lightweight materials by placing PVEH patches on the seven blades of the Wells turbine.

Table 11. All-inclusive forecast of the Wells turbine's total output power from the hybrid energy scheme.

Lightweight Materials	Energy Extracted Through PVEH Patches (W)							CFD 12.10 m/s	Resultant Renewable Power (kW)
	Blade-1	Blade-2	Blade-3	Blade-4	Blade-5	Blade-6	Blade-7		
GFRP-E-Wn	1705	1705	1705	1705	1705	1705	1705		50.07429
CFRP-wet-UD	5148	5148	5148	5148	5148	5148	5148		74.17529
CFRP-UD-Pg	5295	5295	5295	5295	5295	5295	5295		75.20429
CFRP-Wn-Pg	3978	3978	3978	3978	3978	3978	3978		65.98529
CFRP-Wn-wet	3849	3849	3849	3849	3849	3849	3849	38,139.29	65.08229
GFRP-E-UD	2813	2813	2813	2813	2813	2813	2813		57.83029
GFRP-E-wet	2250	2250	2250	2250	2250	2250	2250		53.88929
GFRP-S-UD	2960	2960	2960	2960	2960	2960	2960		58.58929
GFRP-FR-4-Wn	1545	1545	1545	1545	1545	1545	1545		48.95429
KFRP-49-UD	3375	3375	3375	3375	3375	3375	3375		61.76429

4. Conclusions

From this analysis, seven different seven-bladed Wells turbines are designed. Then, CFD analysis for seven different Wells turbine is performed with four different velocities such as 0.34 m/s, 1.54 m/s, 12.10 m/s, and 23 m/s. Through CFD investigation, pressure, velocity, force, and torque are obtained. Using the obtained torque, CASE-IV has a torque of 1729.2 Nm at 23 m/s, and CASE-VI has a torque of 2393.45 at 23 m/s, which are concluded as the optimized Wells turbines. Then, CASE-IV is adopted for the comprehensive structural analyses. The computational structural analyses on the Wells turbine use different lightweight alloys, CFRP, GFRP materials, and few unique composites. From the help of comprehensive structural outcomes, the following observations are obtained: Boron Epoxy is the strongest element because it shows the minimum deformation, stress, and strain compared to other lightweight materials. Compared to CFRP materials, GY-70-Epoxy is considered the strongest element as it has low deformation, stress, and strain. By comparing the GFRP materials, S-Glass-Epoxy-UD is considered the strongest material because it has low deformation, stress, and strain. The shortlisted lightweight materials are used for the hybrid energy calculation. The PVEH-based hybrid energy extraction concept has emerged and has been imposed in this work for various shortlisted lightweight materials. The hydrodynamic medium-based energy extraction from the Wells turbine is listed in Table 10. The hybrid energy concept-based important outcomes are listed in Table 11. From Tables 10 and 11, CASE-VI is a potential case for the enhancement power from hydrodynamic medium as compared to other cases. Finally, a suitable material for high-energy extractions through a hybrid energy mechanism is also found.

Author Contributions: Conceptualization, V.R., J.T. and H.P.J.; methodology, V.R., J.T. and H.P.J.; software, V.R. and P.R.; validation, S.K.M. and H.A.Z.A.-b.; formal analysis, S.K.M., V.R. and P.R.; investigation, S.K.M., R.R., V.R. and P.R.; resources, V.R., R.R., P.R., and S.Z.; data curation, S.K.M., V.R. and P.R.; writing—original draft preparation, S.K.M., P.R. and H.A.Z.A.-b.; writing—review and editing, V.R., P.R., J.T. and S.Z.; visualization, B.S.A., R.R. and S.Z.; supervision, S.K.M., V.R., P.R. and S.Z.; project administration, S.K.M., V.R. and P.R.; funding acquisition, S.Z. and P.R. All authors have read and agreed to the published version of the manuscript.

Data Availability Statement: The authors confirm that the data supporting the findings of this study are available within the article.

Nomenclatures

Design Variables	Explanations
C_{WT}^{B}	Chord length of blade in Wells turbine
$A_{\text{Wells Turbine}}$	Frontal area of the Wells turbine
r_{blade}	Radius of blade in the Wells turbine
$\text{Circum}_{\text{Wells Turbine}}$	Circumference of the Wells turbine
T_{WT}^{B}	Thickness of blade in the Wells turbine
r_{hub}	Radius of hub in the Wells turbine
g	Gravitational force
m_{WT}	Mass of the Wells turbine
C_{WT}	Damping coefficient of the Wells turbine
K_{WT}	Stiffness of the Wells turbine
$F(t)_{\text{Hydrodynamic}}$	Hydrodynamic forces acting on the Wells turbine
u	Displacement
$P_{\text{Intermediate}}^{\text{Hybrid Wells Turbine}}$	Intermediate generated theoretical power from the Wells turbine
$P_{\text{Final}}^{\text{Hybrid Wells Turbine}}$	Final generated theoretical power from the Wells turbine
d_{lwm}	The piezoelectric material constant for PZT is 120.
w	Force acting on the blade of the Wells turbine
f	Natural frequency of the blade of the Wells turbine
$W_{\text{L}-\text{WT}}$	Width of the Wells turbine's blade
L_{PL}	Length of the piezoelectric patches
t_{WT}	Thickness of the Wells turbine's blade
T_{PL}	Thickness of the piezoelectric patches
ε	Dielectric constant of the material
ρ_{lwm}	Density of the base light materials

References

1. Das, T.K.; Kerikous, E.; Venkatesan, N.; Janiga, G.; Thévenin, D.; Samad, A. Performance improvement of a Wells turbine through an automated optimization technique. *Energy Convers. Manag. X* **2022**, *16*, 100285. [CrossRef]
2. Shehata, A.S.; Saqr, K.M.; Xiao, Q.; Shehadeh, M.F.; Day, A. Performance analysis of wells turbine blades using the entropy generation minimization method. *Renew. Energy* **2016**, *86*, 1123–1133. [CrossRef]
3. Barnabei, V.F.; Castorrini, A.; Corsini, A.; Rispoli, F. FSI analysis and simulation of flexible blades in a Wells turbine for wave energy conversion. *E3S Web Conf.* **2020**, *197*, 11008. [CrossRef]
4. Kincaid, K.; MacPhee, D.W. CFD Analysis of stall in a wells turbine. In Proceedings of the ASME 2018 Power Conference POWER 2018, Lake Buena Vista, FL, USA, 24–28 June 2018.
5. Harby, A.H.; Shehata, A.S.; Afify, R.S.; Hanafy, A.A. Experimental investigation for suction slots of wells turbine and shapes of point absorber. *Energy Rep.* **2022**, *8*, 1275–1287. [CrossRef]
6. Gareev, A.; Cooper, P.; Kosasih, P.B. *CFD Analysis of Air Turbines as Power Take-Off Systems in Oscillating Water Column Wave Energy Conversion Plant*; University of Wollongong: Wollongong, NSW, Australia, 2009.
7. Shehata, A.S.; Xiao, Q.; Saqr, K.M.; Alexander, D. Wells turbine for wave energy conversion: A review. *Int. J. Energy Res.* **2016**, *41*, 6–38. [CrossRef]
8. Karthick, N.; Sanjai, M. Optimization of the Wells Turbine by using Slotted blade and Guide Vanes. *Int. J. Creat. Res. Thoughts* **2018**, *6*, 969–978.
9. Suzuki, M.; Arakawa, C. Flowon Blade of Wells Turbine for Wave Power Generation. *J. Vis.* **2006**, *9*, 83–90. [CrossRef]
10. Thakker, A.; Abdulhadi, R. The performance of Wells turbine under bi-directional airflow. *Renew. Energy* **2008**, *33*, 2467–2474. [CrossRef]
11. Torresi, M.; Camporeale, S.M.; Pascazio, G.; Fortunato, B. Fluid Dynamic Analysis of a Low Solidity Wells Turbine. In Proceedings of the 59 Congresso ATI, Genova, Italy, 14–17 October 2004.
12. Torresi, M.; Camporeale, S.M.; Pascazio, G. Performance of a small prototype of a highsolidity wells turbine. In Proceedings of the 7th European Conference on Turbomachinery: Fluid Dynamics and Thermodynamics (ETC, 2007), Athens, Greece, 5–9 March 2007.

13. Dorrell, G.; Hsieh, M.-F. Performance of Wells Turbines For Use In Small-Scale Oscillating Water Columns. Available online: https://onepetro.org/ISOPEIOPEC/proceedings/ISOPE08/All-ISOPE08/ISOPE-I-08-165/10667 (accessed on 6 July 2008).

14. Sharma, S.; Peng, S.-L.; Agrawal, J.; Shukla, R.K.; Le, D.-N. *Data, Engineering and Applications*; Springer Nature: Berlin/Heidelberg, Germany, 2022.

15. Curran, R.; Gato, L.M.C. The energy conversion performance of several types of Wells turbine designs. *Proc. Inst. Mech. Eng. Part A J. Power Energy* **1997**, *211*, 133–145. [CrossRef]

16. Lekube, J.; Garrido, A.; Garrido, I.; Otaola, E.; Maseda, J. Flow Control in Wells Turbines for Harnessing Maximum Wave Power. *Sensors* **2018**, *18*, 535. [CrossRef]

17. Halder, P.; Samad, A.; Thévenin, D. Improved design of a Wells turbine for higher operating range. *Renew. Energy* **2017**, *106*, 122–134. [CrossRef]

18. Watterson, J.K.; Raghunathan, S. Numerical Analysis of Wells Turbine Aerodynamics. *J. Propuls. Power* **1999**, *15*, 253–259. [CrossRef]

19. Torresi, M.; Stefanizzi, M.; Fornarelli, F.; Gurnari, L.; Filianoti, P.G.F.; Camporeale, S.M. Performance characterization of a wells turbine under unsteady flow conditions. In Proceedings of the Second International Conference on Material Science, Smart Structures and Applications: ICMSS-2019, Erode, India, 20–21 November 2019. [CrossRef]

20. Taha, Z.; Sugiyono; Sawada, T. A comparison of computational and experimental results of Wells turbine performance for wave energy conversion. *Appl. Ocean Res.* **2010**, *32*, 83–90. [CrossRef]

21. Samad, A. Effect of guide vane angle on wells turbine performance. In Proceedings of the ASME 2014 Gas Turbine India Conference, GTINDIA, New Delhi, India, 15–17 December 2014. [CrossRef]

22. Valizadeh, R.; Abbaspour, M.; TaeibiRahni, M.; Pour, M.S.; Hulme-Smith, C. Improved Wells Turbine Using a Concave Sectional Profile. *Preprints* **2020**, 2020100045. [CrossRef]

23. Cruz, J. *Ocean Wave Energy: Current Status and Future Prespectives*; Springer: Berlin/Heidelberg, Germany, 2008.

24. Oaly, J.; Frawley, P.; Thakker, A. A 2-D computational fluid dynamics analysis of wells turbine blade profiles in isolated and cascade flow. In Proceedings of the OMAEí02 21st International Conference on Offshore Mechanics and Arctic Engineering, Oslo, Norway, 23–28 June 2002.

25. Kumar, P.M.; Samad, A. Nature-inspired design of a turbine blade harnessing wave energy. *Proc. Inst. Mech. Eng. Part A J. Power Energy* **2019**, *234*, 670–689. [CrossRef]

26. Cambuli, F.; Ghisu, T.; Virdis, I.; Puddu, P. Dynamic interaction between OWC system and Wells turbine: A comparison between CFD and lumped parameter model approaches. *Ocean Eng.* **2019**, *191*, 106459. [CrossRef]

27. Torresi, M.; Camporeale, S.M.; Pascazio, G. Detailed CFD Analysis of the Steady Flow in a Wells Turbine Under Incipient and Deep Stall Conditions. *J. Fluids Eng.* **2009**, *131*, 071103. [CrossRef]

28. Torresi, M.; Camporeale, S.M.; Pascazio, G. Experimental and numerical investigation on the performance of a wells turbine prototype. In Proceedings of the 7th European Wave and Tidal Energy Conference, Porto, Portugal, 11–13 September 2007.

29. Ghisu, T.; Puddu, P.; Cambuli, F. A detailed analysis of the unsteady flow within a Wells turbine. *Proc. Inst. Mech. Eng. Part A J. Power Energy* **2017**, *231*, 197–214. [CrossRef]

30. Torresi, M.; Stefanizzi, M.; Gurnari, L.; Filianoti, P.G.F.; Camporeale, S.M. Experimental characterization of the unsteady performance behavior of a Wells turbine operating at high flow rate coefficients. *E3S Web Conf.* **2020**, *197*, 08009. [CrossRef]

31. Kotb, A.T.M.; Nawar, M.A.A.; Attai, Y.A.; Mohamed, M.H. Performance optimization of a modified Wells turbine for wave energy conversion. *Ocean Eng.* **2023**, *280*, 114849. [CrossRef]

32. Morais, F.J.F.; Carrelhas, A.A.D.; Gato, L.M.C. Biplane-rotor Wells turbine: The influence of solidity, presence of guide vanes and comparison with other configurations. *Energy* **2023**, *276*, 127514. [CrossRef]

33. Stefanizzi, M.; Camporeale, S.M.; Torresi, M. Experimental investigation of a Wells turbine under dynamic stall conditions for wave energy conversion. *Renew. Energy* **2023**, *214*, 369–382. [CrossRef]

34. Zarketa-Astigarraga, A.; Martin-Mayor, A.; Maeso, A.; de Miguel, B.; Martinez-Agirre, M.; Penalba, M. A holistic optimization tool for the design of power take-off systems in realistic wave climates: The Wells turbine case. *Ocean Eng.* **2023**, *285*, 115332. [CrossRef]

35. Geng, K.; Yang, C.; Zhao, B.; Zhao, W.; Gao, J.; Hu, C.; Zhang, H.; Wu, W. Residual circulation budget analysis in a Wells turbine with leading-edge micro-cylinders. *Renew. Energy* **2023**, *216*, 119049. [CrossRef]

36. Kotb, A.T.M.; Nawar, M.A.A.; Attai, Y.A.; Mohamed, M.H. Performance assessment of a modified wells turbine using an integrated casing groove and Gurney flap design for wave energy conversion. *Renew. Energy* **2022**, *197*, 627–642. [CrossRef]

37. Raja, V.; Prakash, R.A.; Kumar, A.; de Pacheco, D.A.J. Multi-disciplinary engineering design of a high-speed nature-inspired unmanned aquatic vehicle. *Ocean Eng.* **2023**, *270*, 113455. [CrossRef]

38. Raja, V.; Murugesan, R.; Rajendran, P.; Palaniappan, S.; Al-Bonsrulah, H.A.Z.; Jayaram, D.K.; Al-Bahrani, M. Multi-Domain Based Computational Investigations on Advanced Unmanned Amphibious System for Surveillances in International Marine Borders. *Aerospace* **2022**, *9*, 652. [CrossRef]

39. Raja, V.; Madasamy, S.K.; Rajendran, P.; Ganesan, S.; Murugan, D.; Al-Bonsrulah, H.A.Z.; Al-Bahrani, M. Nature-Inspired Design and Advanced Multi-Computational Investigations on the Mission Profile of a Highly Manoeuvrable Unmanned Amphibious Vehicle for Ravage Removals in Various Oceanic Environments. *J. Mar. Sci. Eng.* **2022**, *10*, 1568. [CrossRef]

40. Kumar, K.N.; Meenakshi, S.; Deviparameswari, K.; Vaidegi, R.; Nandhagopal, R.; Ramesh, M.; Vijayanandh, R. Investigation of energy generation on large rotary wing unmanned aerial vehicle's propeller using coupled engineering approaches. In *Advances in Environment Engineering and Management*; Springer: Cham, Switzerland, 2021; pp. 209–224.

41. Gnanasekaran, R.K.; Shanmugam, B.; Raja, V.; Al-Bonsrulah, H.A.Z.; Rajendran, P.; Radhakrishnan, J.; Eldin, S.M.; Narayanan, V. Comprehensive computational investigations on various aerospace materials under complicated loading conditions through conventional and advanced analyses: A verified examination. *Front. Mater.* **2023**, *10*, 1147310. [CrossRef]

42. Wang, Y.; Kumar, L.; Raja, V.; AL-bonsrulah, H.A.Z.; Kulandaiyappan, N.K.; Amirtharaj Tharmendra, A.; Marimuthu, N.; Al-Bahrani, M. Design and Innovative Integrated Engineering Approaches Based Investigation of Hybrid Renewable Energized Drone for Long Endurance Applications. *Sustainability* **2022**, *14*, 16173. [CrossRef]

43. Kulandaiyappan, N.K.; John, B.R.R.; Raja, V. Investigation of Aeroelastic Energy Extraction from Cantilever Structures under Sustained Oscillations. *Processes* **2023**, *11*, 830. [CrossRef]

44. Raja, V.; Al-Bonsrulah, H.A.Z.; Raji, A.P.; Madasamy, S.K.; Ramaiah, M.; Gnanasekaran, R.K.; Kulandaiyappan, N.K.; Al-Bahrani, M. Design and multi-disciplinary computational investigations on PVEH patches attached horizontal axis hybrid wind turbine system for additional energy extraction in HALE UAVs. *IET Renew. Power Gener.* **2023**, *17*, 617–643. [CrossRef]

45. Morada, A.M.; Elzahaby, A.; Abdallah, S.; Kameld, M.; Khalile, M.K. Application of Piezoelectric Materialsfor Aircraft Propeller Blades Vibration Damping. *Int. J. Sci. Eng. Res.* **2015**, *6*, 513–520.

46. Du, S.; Jia, Y.; Seshia, A. Maximizing Output Powerina Cantilevered Piezoelectric Vibration Energy Harvester by Electrode Design. *J. Phys. Conf. Ser.* **2015**, *660*, 012114. [CrossRef]

47. Dunnmon, J.; Stanton, S.; Mann, B.; Dowell, E. Power extraction from aeroelastic limit cycle oscillations. *J. Fluids Struct.* **2011**, *27*, 1182–1198. [CrossRef]